UNIVERSITA' DEGLI STUDI DI PADOVA

Dipartimento di Fisica e Astronomia "Galileo Galilei"

Master Degree in Astrophysics and Cosmology

Final Dissertation

Spatially resolved scaling relations in nearby galaxies: stellar Mass assembly constraints from their star formation histories

Thesis supervisor
Prof.ssa Giulia Rodighiero
Thesis co-supervisor
Dott. Andrea Enia

Candidate

Cristina Maria Lofaro

Academic Year 2020/21

Contents

Chapter 1

Introduction

1.1 Setting the framework: the main sequence relation of star-forming galaxies

Galaxies appear to build their stellar masses in a steady mode mainly dominated by secular processes and thanks to the accretion of cold gas. This picture finds its confirmation in the existence of a tight relation between the galaxy stellar mass (M_*) and its star formation rate (SFR): the Main Sequence (MS) of star-forming galaxies (SFGs), observed up to $z \sim 6$ with a fairly constant scatter of $\sim$0.3 dex (e.g. Noeske et al. 2007; Daddi et al. 2007; Rodighiero et al. 2014; Speagle et al. 2014; Whitaker et al.2014; Schreiber et al. 2015; Renzini & Peng 2015; Popesso et al. 2019). Galaxies seem to oscillate around the MS relation as a consequence of multiple events of central compaction of gas followed by inside-out gas depletion, thus related with the flows of cold gas in galaxies (Tacchella et al. 2015). Several works in the recent years exploited the MS relation as a reference to understand the differences among galaxies characterised by different rates of stellar production (starbursts, SFGs, passive galaxies), with the final aim of understanding the origins of galaxy bimodality, and how the star formation activity is quenched (e.g. Rodighiero et al. 2011; Peng et al. 2015; Saintonge et al. 2016). The existence of a tight relation between stellar mass surface density (Σ_*) and star formation rate surface density ($\Sigma(SFR)$) found in HII regions of nearby galaxies, further suggests that the global MS relation originates thanks to local processes that set the conversion of gas into stars
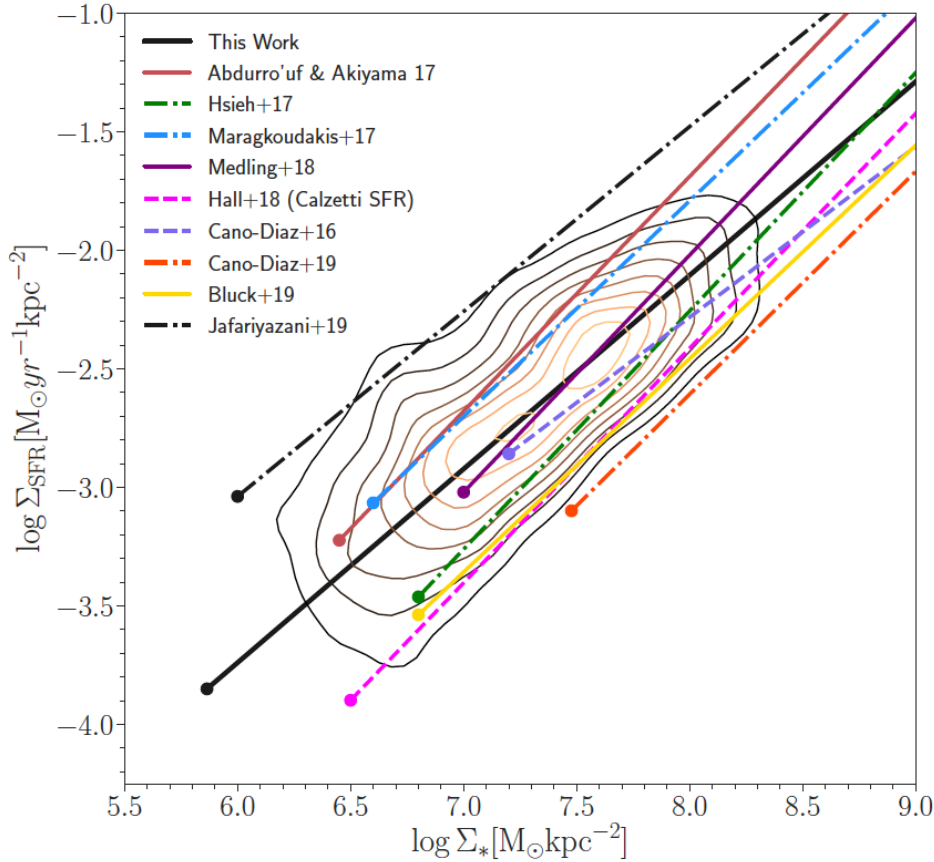
Figure 1.1: Collection of resolved MS relations from the literature. Each relation, that has been converted to a Chabrier (2003) IMF, and re-scaled to $z = 0$ starts from the sensitivity limit reported in the parent study (from Enia et al. 2020).

(Rosales-Ortega et al. 2012; Sanchez et al. 2013). Following this, several works exploited the advent of large integral field spectroscopic (IFS) surveys to analyse the existence of a spatially resolved MS relation at low redshift, using the $H\alpha$ flux as SFR tracer (e.g. Cano-Diaz et al. 2016, Hsieh et al. 2017, Abdurro'uf & Akiyama 2017, Medling et al. 2018, Cano-Dıaz et al. 2019). These studies found that the slope of the relation varies dramatically (from 0.3 to 0.99 in log space) depending on the SFR tracer, on the source selections, on the mathematical method to perform the statistical fitting analysis (see Figure 1.1 for a summary of the main resolved Main Sequences reported in the literature).

1.2 A panchromatic approach

To homogenize all these observational results into a coherent scenario, it is mandatory to account for the different selection samples and for potential systematics in the methodology adopted to compute the galaxy physical parameters. To this aim, Enia et al. (2020) tried to cope with the main biases affecting the bulk of the previous works that are almost based on emission lines (i.e. $H\alpha$) or UV-to-optical tracers to constrain the SFR (see Sanchez et al., 2019 for a review). With such an approach, it turns possible to exploit the power of a complete multiwavelength photometric coverage, extending from the far-UV up to the far-IR (i.e. from GALEX to Herschel) to provide a reliable measure of the comprehensive SFR in galaxies, directly accounting for both the observed and the obscured components. This can be performed by an SED fitting procedure, that, accounting for an energetic balance, allows to go deeper than spectroscopic surveys based on $H\alpha$ emission lines. The latter critically depend on dust extinction corrections derived from the Balmer decrement and mostly on the spectral Signal-to-Noise ratio (SNR) limit needed (for example) for the spaxels classification on BPT diagrams, requiring significant detection of four emission lines. Thus, exploitation of the higher SNR of the photometric data that will allow us to reach the farthest galactocentric distances, and the combination of UV and far-Infrared measurements to minimize the uncertainties related to the presence of dust.

1.2.1 An unexploited multiwavelength dataset

Gas makes up $\sim$99% of the mass of the interstellar medium (ISM, $\sim$74% of hydrogen, $\sim$25% of helium and $\sim$1% of heavier elements, generically named 'metals') and the remaining $\sim$1% is as dust. The ISM is of vital importance for the lifecycle of galaxies thanks to its ability to condense and form stars, and to be regenerated by stellar evolution. Star formation (SF) takes place within dense molecular clouds (e.g., Krumholz et al., 2011) and stars return the products of their evolution through stellar winds and supernova explosions (e.g., Veilleux et al., 2005). Although dust constitutes a small percentage of the ISM, understanding its properties is of particular importance for several reasons. The formation of hydrogen molecules (H2), the raw material for SF, occurs on the surface of dust grains (Gould & Salpeter, 1963). Dust

affects our view of galaxies at different wavelengths, by absorbing the ultraviolet (UV) and optical light and re-emitting it in the infrared (IR). Correcting for dust extinction is usually the main source of uncertainty when we derive properties such as star-formation rate (SFR), age, or metallicity (e.g., Calzetti, 2001). In addition, dust plays a major role for understanding the chemical evolution of galaxies. Metals produced by stellar nucleosynthesis are returned to the ISM and provide most of the cooling to create a new generation of stars. They can be found either in gaseous form or as solid grains condensed during the final stages of stellar evolution. Dust grains can later be destroyed and incorporated in the gas phase or in the next generation of stars. The dust-to-gas mass ratio (DGR) is indeed an alternative way to measure the metal content of galaxies. The project "DustPedia - A definitive study of Cosmic Dust in the local Universe" (www.dustpedia.com; Davies et al., 2017) is supported by the EU FP7 grant 606847 (PI: J. Davies, Cardiff University). The goal of DustPedia is to perform a complete characterization of dust in local galaxies including: its composition and physical properties in different galactic environments; its origin and evolution; its relation to other ISM components; its effects on stellar radiation; the connection between SF indicators and dust emission; the contribution of local galaxies to the cosmic far-IR background. The research is carried out on a sample of 875 objects, i.e. all the large (D25 > 1') and nearby ($z < 0.01$) galaxies observed by the Herschel Space Observatory. A legacy database was constructed from Herschel and other UV-to-microwave observations (Clark et al., 2018), containing multiwavelength imagery and aperture-matched photometry in up to 42 bands (25 bands available, on average, for a DustPedia galaxy). This rich database is currently being analyzed with a variety of theoretical models to fit the global Spectral Energy Distribution, to study the details of local radiative transfer and energy budget and to understand the variation of dust properties with environment. More details on Dustpedia will be presented in Chapter 2.

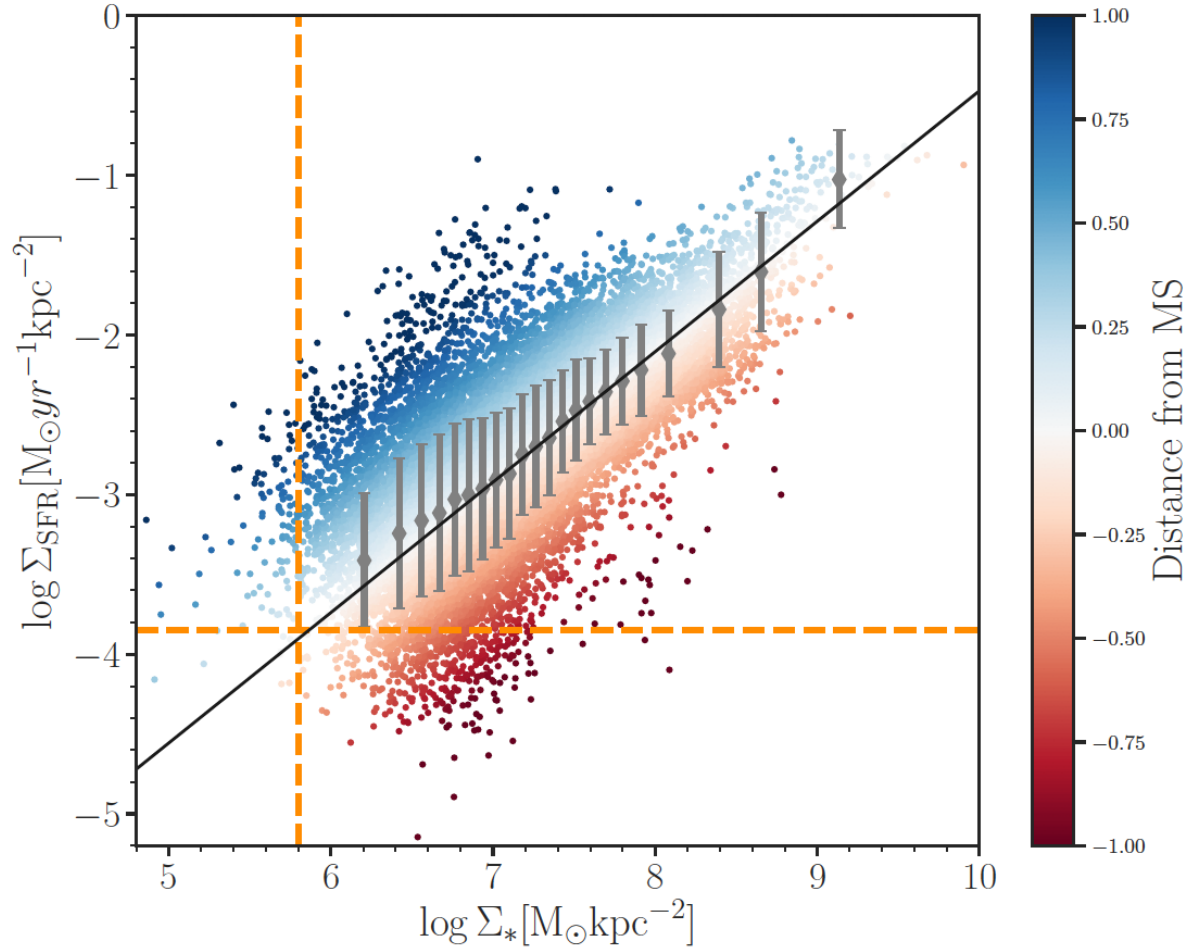Figure 1.2: The resolved main sequence for local grand design spirals. 8" cells results for star formation rate surface density and stellar mass density, color coded as a function of their distance from the main sequence. Orange dashed lines are the sensitivity limits. The MS (black solid line) is obtained as the linear fit of the gray data points. The error bars are the dispersion in each bin (from Enia et al. 2020).

1.3 The Main Sequence of star-forming galaxies constrained by Dustpedia

As mentioned in the first Section, the star-forming main sequence is a well studied tight relation between stellar masses and star formation rates, observed up to $z \sim 6$, over a great variety of environments and morphologies, both globally, counting galaxies as a whole, and locally, resolving physical properties in single galaxy regions. In a recent paper, Enia et al. (2020) have performed a spatially resolved SED fitting in a sample of 8 local grand-design spirals taken from the DustPedia archive and they used the outputted maps of stellar mass and star formation rate to analyse the spatially resolved Main Sequence (MS) of star-forming galaxies (SFGs) on scales spanning the range between 0.4-1.5 kpc. We summarise here their main findings:

• When considering the 8 galaxies together, they obtain a spatially resolved Main Sequence with a slope of 0.82 and an intercept of -8.69 (Figure 1.2). When fitting the data with the ODR method we obtain a slope and an intercept of 0.88 and -9.05, respectively. This relation holds on different scales, from sub-galactic to galactic (see Figure 1.3;

• The local spatially resolved MS is consistent with the normalized low-mass high-redshift relation, thus proving its universality across cosmic time. This is a crucial point to validate the integrated information on single galaxies at high redshift;

• This approach allows to overtake the limits of all the spectroscopic resolved emission lines studies, based mainly on $H\alpha$ and Balmer decrement corrections for dust extinction. The sensitivities of these surveys do not sample the lowest M_* and SFR as they do with a multi-wavelength photometric approach, allowing to probe the outermost regions of galaxies (see example in Figure 1.4). The combination of all the eight galaxies demonstrates the existence of a universal relation, as the deviation of single sources is well within the global scatter of -0.27 dex. Such relation holds at different galaxy scales, supporting the interpretation from other surveys that the SFR is regulated by local processes of gas-to-stars conversion happening at GMC scales on the order of a few hundred pc. With respect to other works, Enia et al. (2020), however, provided evidence that such secular regulation keeps to apply at the farthest galactocentric distances, where the optical disk is still influenced by the density waves
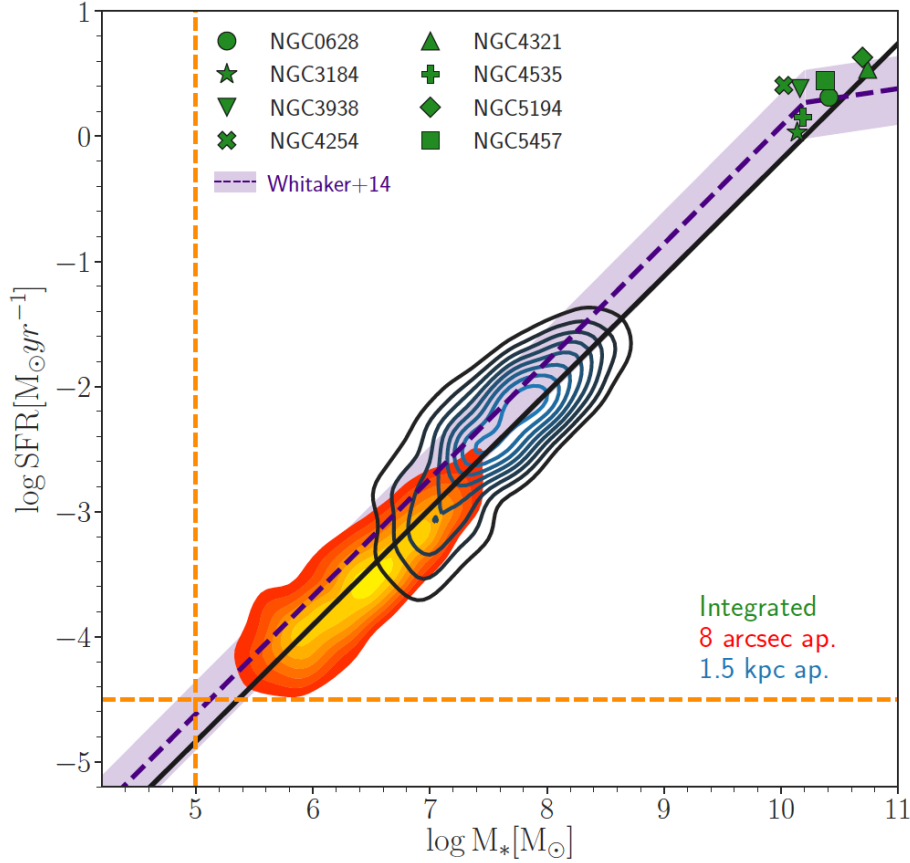
Figure 1.3: Sample properties evaluated in three different apertures. In green, the integrated properties, obtained fitting the available photometry in apertures containing the full galaxy emission. Marker size is as big as the data error bars. Blue and filled red contours are referred to cells of 1.5 kpc and 800 respectively. Black line is the fit to the MS described by the 800 results. Purple dashed line is the MS relation from Whitaker et al. (2014) rescaled at z=0, while the shaded area enclose the scatter of MS distribution we obtain (0.27 dex). Dashed orange lines are the stellar mass and SFR sensitivity limit (from Enia et al. 2020).

motions, originating the spiral arms. This work defines an accurate locus in the $\Sigma(SFR)$-Σ_* plane (see Figure 1), constrained by observed distributions covering 3dex in the parameters space. Such a definition of the spatially resolved MS in local disk galaxies will represent a valuable reference for future comparison to different galaxy morphological types adopting a similar panchromatic approach.

1.4   Motivation of this Thesis

The sample presented in Enia et al. (2020) is very conservative, given that it is restricted to the grand design spirals with low inclination, large spatial extension and regular spiral arms structures in DustPedia. This analysis has provided a total of tens of thousands of physical cells on typical scales of ~0.5 kpc over very different internal galaxy environments (bulges, spiral arms, interarms regions, outskirts). This set is thus very important to study the secular evolution processes that regulate star formation in local sources, dominated by rotationally supported systems (e.g. Law et al. 2009; Forster-Schreiber et al. 2009; Glazebrook 2013; Wisnioski et al. 2015; Simons et al. 2017; Forster-Schreiber et al. 2018; Übler et al. 2019). However, single galaxies show peculiar variations around the $\Sigma(SFR)$-Σ_* relation, indicating that a comprehensive analysis of a larger sample of sources will be required to fully understand how secular (disks) vs stochastic (merger) processes shape the large variety of morphological galaxy types that we observe in the local Universe. The original plan of my Thesis was to extend this analysis on different morphological types.

However, we thought that Star Formation Histories (SFHs) are a fundamental tool to reveal the galaxy path from the earlier stages of formation to the present time. The various phases of galaxy evolution are imprinted in the source spectrum, globally and locally. Thus, it becomes possible to reconstruct a galaxy history, i.e. detecting past interactions with other galaxies, or disentangling the formation histories of the single stellar populations (see Walcher et al. 2011 for a review). Multiple tools are available to reconstruct the SFH of a galaxy (or a resolved region) from its panchromatic flux (i.e. MAGPHYS, Bagpipes). In this work I have then extended the analysis in Enia et al. (2020) in order to extract the SFHs in a very small subset of galaxies. Three of the galaxies in the original sample (NGC4321, NGC4535 and NGC5194)
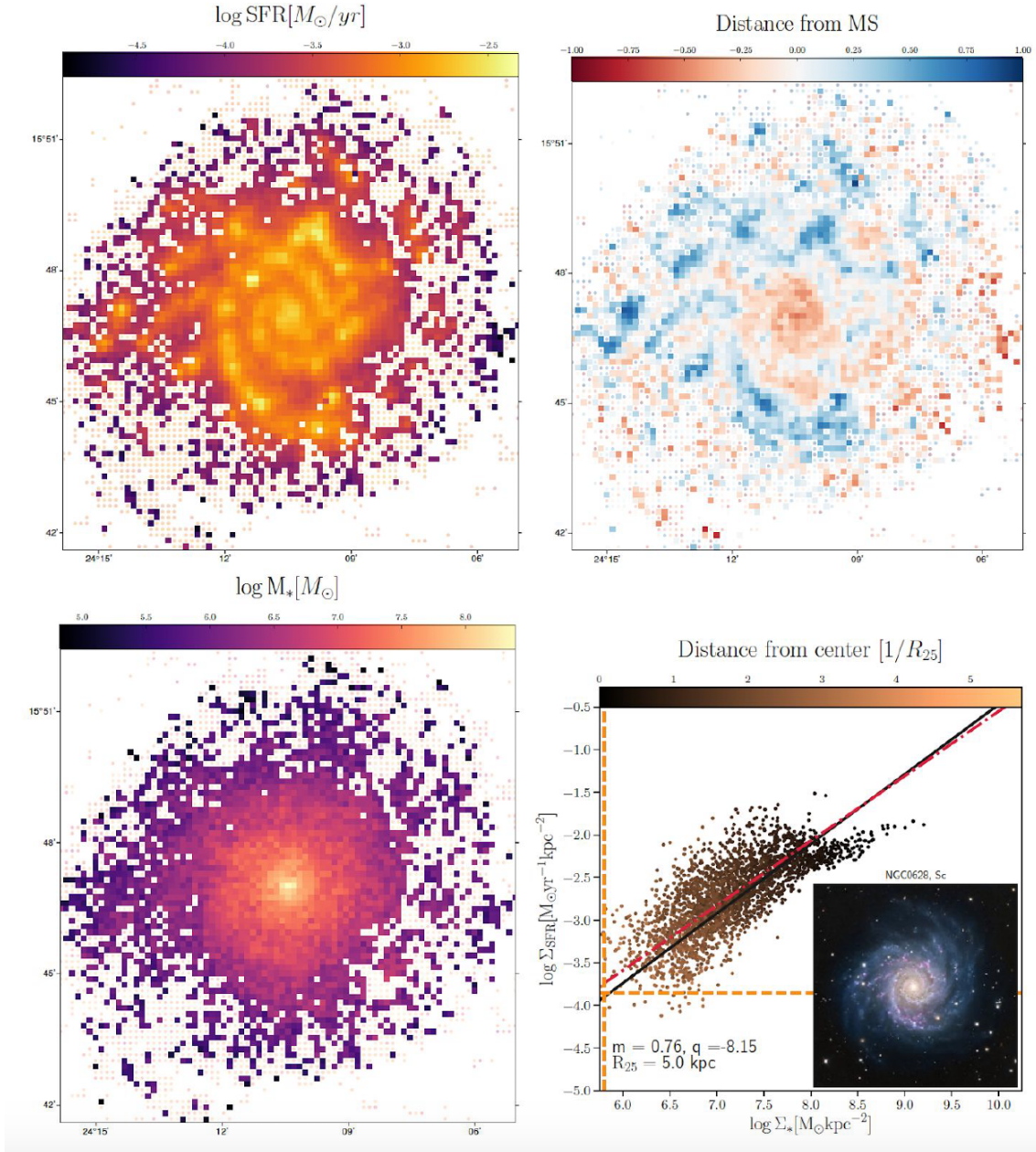
Figure 1.4: Example of NGC0628, based on the analysis of Dustpedia for NGC0628. Panels are organized as follows: upper left, the cells in log(star formation rate); upper right, the cells distance from the MS; lower left, the cells log stellar mass; lower right, how the galaxy cells are positioned in the M_*-SFR plot, color-coded according to the distance from the galaxy center in units of R25. Black line is the (total fitted) MS, red dashed line the ODR fit for the single galaxy points, orange lines the sensitivity limits, the inset an RGB image of the galaxy as observed in optical bands. In the first three panels, cells rejected for having a χ^2 over the threshold are shown as points (from Enia et al. 2020).

hint at the presence of a quenched ring in the galaxy outskirts, that seems to translate into a sequence below the main one. Knowing the SFH of those external regions is fundamental to assess the typical ages of their stellar populations (i.e. an older population goes toward the confirmation of the presence of a quenched ring generating a second sequence) and to disentangle between in-situ and ex-situ galaxies formation models. Moreover, the same spatially resolved SFH analysis extended to a sample of galaxies on their way to be quenched (identified from the full Dustpedia sample as shown in point one) is able to identify the "direction" of the quenching processes, distinguishing between outside-in or inside-out quenching processes.

Chapter 2

DUSTPEDIA

Dustpedia is a research project aimed at the characterization of the dust in the local universe. Posed as the legacy of the Hershel Space Observatory, it contains the imagery and photometry study of 875 nearby galaxies, spanning over five orders of magnitude in wavelength, from ultraviolet to microwave (Fig.2.1), and was made publicly available to the scientific community through the Dustpedia database. Subsequently the considerable data improvement
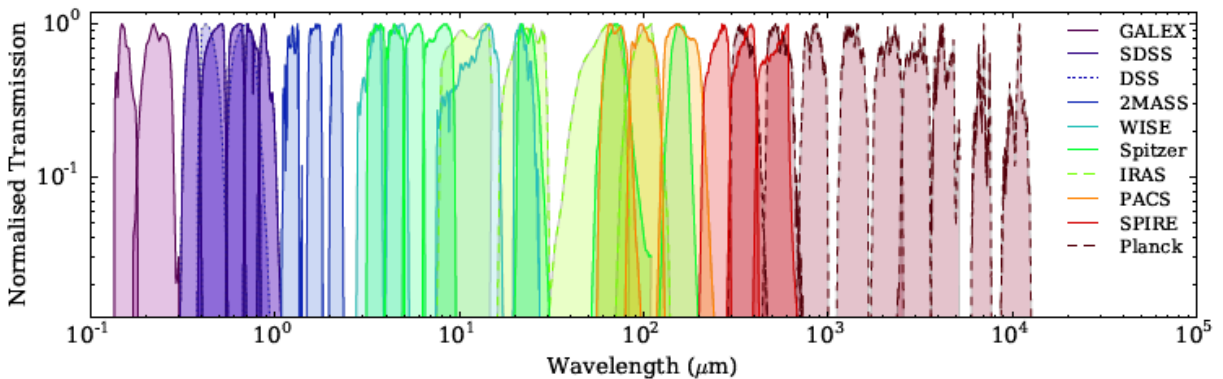
Figure 2.1: Illustration of the spectral coverage provided by the DustPedia database, showing filter response functions of all the bands treated. As can be seen, the complete sampling covers about more than five orders of magnitude.

of the last years and exploration of a wide spectral range (from far-infrared up to the sub-millimetre) through the Herschel, Planck, Spitzer, the James Clerk Maxwell Telescope (JCMT) and the recent Atacama Large Millimetre/sub-millimetre Array (ALMA) observatories, a rele-

vant development in the cosmic dust investigation was possible. Among the above-mentioned observatories, Hershel, in particular, was well suited for the study of nearby galaxies due to its rapid mapping abilities enabled it to observe a sizeable portion of the galaxies in the local universe mixing up sensitivity, resolution, and broad wavelength coverage.

The sample consists of galaxies observed within 41 Mpc distance assuming H_0=73.24 km/s/Mpc and D25 > 1′. For the intend of measuring dust, the available instruments, adopted in modern extra-galactic astronomy, are such that it is possible to compare extensive multi-wavelength data even though they have various origins. This is true for different spectral energy distribution coding tools which take advantage of this modern technique: MAGPHYS, CIGALE, SKIRT and so on: for example, in energy-balance SED-fitting, the stellar population sampled by ultraviolet (UV), optical and near-infrared data points is the same stellar population heating the dust observed at mid infrared to sub-millimetre wavelengths (Fig. 2.2).
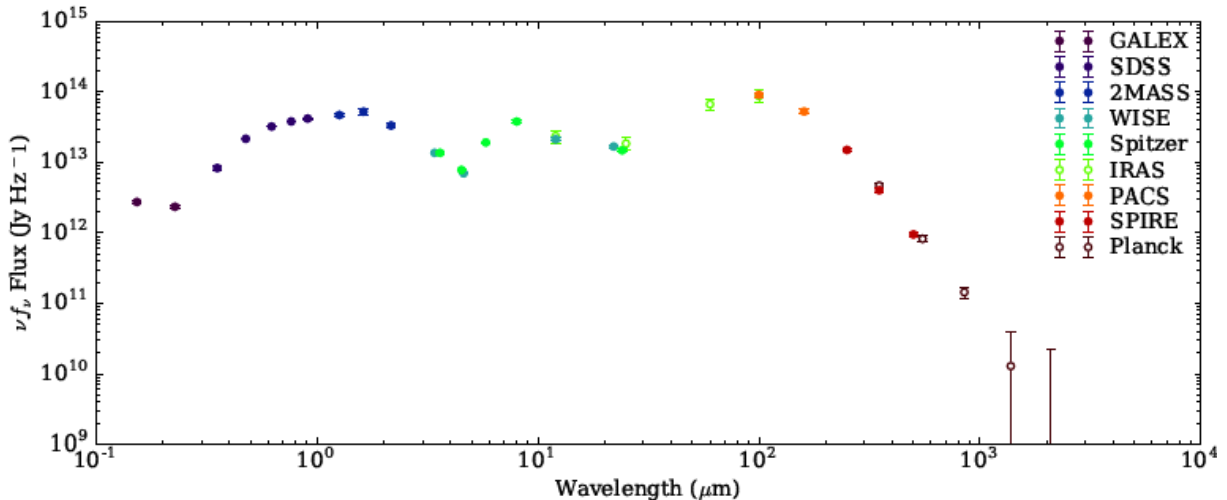

Figure 2.2: Example of a UV–mm SED of NGC3683, demonstrating the rich photometric coverage possible for the DustPedia galaxies.

2.1   Multi-wavelength imagery

For the nearby galaxies sampled in the Dustpedia database, the Herschel-SPIRE and Herschel-PACS maps reductions are produced in the Flexible Image Transport System format (FITS.file);

in particular the file name shows the target galaxy, facility, and the band considered. However, the FITS headers contain the standard World Coordinate System fields, along with fields providing a range of additional information (besides the target galaxy): telescope, filter effective wavelength, filter name, instrument, map units and the name of the database the original data was taken from. The file can include the image map or the error map, conveniently specified, both in units of Jy/pix. The Jansky is a non-SI unit of spectral flux density used especially in radio astronomy:

$$1 Jy = 10^{-23} \frac{erg}{s \ cm^2 \ Hz} \tag{2.1}$$

or

$$1 Jy = 10^{-26} \frac{W}{m^2 \ Hz}. \tag{2.2}$$

2.1.1 Ancillary Imagery

The ancillary imaging data consists of observations from 8 facilities; the GALaxy Evolution eXplorer (GALEX; Morrissey et al. 2007), the Sloan Digital Sky Survey (SDSS; York et al. 2000; Eisenstein et al. 2011), the Digitized Sky Survey (DSS), the 2 Micron All-Sky Survey (2MASS; Skrutskie et al. 2006), the Wide-field Infrared Survey Explorer (WISE; Wright et al.2010), the Spitzer Space Telescope, (Werner et al. 2004), and Planck (Planck Collaboration et al. 2011) as shown in Fig. 2.3.

GALEX

The ultraviolet part of the electromagnetic spectrum is sampled by GALEX. GALEX data are divided in near-UV (NUV, 1516 Å) and FUV (2267 Å). NUV and FUV data sample the light coming from newborn massive stars, tracing the unobscured star formation activity of galaxies. GALEX coverage is available for the vast majority of the DustPedia Herschel galaxies; 797 (91%) in FUV and 832 (95%) in NUV. The original GALEX tile pixel units of counts/s/pix were translated to Jy/pix using conversion factors of $1.076 \ x10^{-4}$ Jy s/counts in the FUV and $3.373 \ x10^{-5}$ Jy s/counts in the NUV.

Facility	Effective Wavelength	Band Name	Imagery Present	Photometry Present	Pixel Width (″)	Resolution FWHM (″)	Calibration Uncertainty (%)	
GALEX	153 nm	FUV	797	794	3.2	4.3	4.5	a
GALEX	227 nm	NUV	832	830	3.2	5.3	2.7	
SDSS	353 nm	u	655	655	0.45	1.3	1.3	
SDSS	475 nm	g	655	655	0.45	1.3	0.8	
SDSS	622 nm	r	655	655	0.45	1.3	0.8	b
SDSS	763 nm	i	655	655	0.45	1.3	0.7	
SDSS	905 nm	z	655	655	0.45	1.3	0.8	
DSS1	450 nm	B	794	–	1–1.7	1.9 (1.5–3.0)	–	
DSS1	660 nm	R	794	–	1–1.7	1.9 (1.5–3.0)	–	
DSS2	450 nm	B	861	–	1–1.7	1.9 (1.5–3.0)	–	
DSS2	660 nm	R	861	–	1–1.7	1.9 (1.5–3.0)	–	
2MASS	1.24 μm	J	875	875	1	2.0	1.7	
2MASS	1.66 μm	H	875	875	1	2.0	1.9	c
2MASS	2.16 μm	K_S	875	875	1	2.0	1.9	
WISE	3.4 μm	(W1)	875	875	1.375	6.1	2.9	
WISE	4.6 μm	(W2)	875	875	1.375	6.4	3.4	d
WISE	12 μm	(W3)	875	875	1.375	6.5	4.6	
WISE	22 μm	(W4)	875	875	1.375	12	5.6	
Spitzer	3.6 μm	(IRAC-1)	644	623	0.75	1.66	3	
Spitzer	4.5 μm	(IRAC-2)	804	777	0.75	1.72	3	
Spitzer	5.8 μm	(IRAC-3)	392	374	0.6	1.88	3	e
Spitzer	8.0 μm	(IRAC-4)	411	392	0.6	1.98	3	
Spitzer	24 μm	(MIPS-1)	491	477	2.4–2.6	6	5	
Spitzer	70 μm	(MIPS-2)	198	177	4	18	10	f
Spitzer	160 μm	(MIPS-3)	184	171	8	38	12	
PACS	70 μm	–	255	244	2	9 (5.8–12.2)	7	
PACS	100 μm	–	716	701	3	10 (6.9–12.7)	7	g
PACS	160 μm	–	771	753	4	13 (12.1–15.7)	7	
SPIRE	250 μm	(PSW)	844	844	6	18	5.5	
SPIRE	350 μm	(PMW)	844	844	8	25	5.5	h
SPIRE	500 μm	(PLW)	844	844	12	36	5.5	

Figure 2.3: Details of each band for every data of the 875 nearby galaxies in the Dustpedia Database.

SDSS

The Sloan Digital Sky Survey (SDSS) provides ultraviolet, optical, and near-infrared imaging of the 35% of the sky. Sampling the young stellar content, it is probed with the Data Release 12 of SDSS in the *u,g,r,i,z* bands with, respectively, effective wavelengths of 3351 Å, 4686 Å, 6166 Å, 7480 Åand 8932 Å.

2MASS

The 2 Micron All-Sky Survey (2MASS) provides near-infrared imaging of the entire sky in J-band, H-band, and K_S-band, respectively at 1.25μm, 1.65μm and 2.16 μm. 2MASS dataset was acquired from the NASA/IPAC Infrared Science Archive (IRSA17). 2MASS-H band photometry might be affected by a distinctive offset with respect to J and K_S-band photometry, translating as a "bump" or "dip" in the SED of the object.

WISE

The Wide-field Infrared Survey Explorer (WISE) provides near-infrared and mid-infrared coverage of the entire sky with the WISE camera on board of Spitzer at 3.4μm, 4.6μm, 12μm and 22μm. NIR and MIR observations trace the old stellar component, the stellar mass distribution and the carbonaceous-to-silicate materials in the dust.

SPITZER

Also the Spitzer Space Telescope covers the same wide spectral range of WISE (from NIR up to FIR across seven photometric bands) provided by two cameras: the InfraRed Array Camera (IRAC) detecting at 3.6μm, 4.5μm, 5.8μm, 8.0μm and the Multiband Imager for Spitzer (MIPS) at 24μm, 70μm and 160μm. The pixel units of all maps were converted from MJy/sr to Jy/pix. Furthermore, 826 of the DustPedia galaxies (94% of the total) have Spitzer coverage in at least one photometric band, 808 (92%) have IRAC coverage, whilst 493 (56%) have MIPS coverage.

HERSCHEL

Directly from the instruments on board the Herschel Space Observatory, it is possible to obtain data points from the far-infrared up to the sub-mm through both Herschel PACS at 70μm, 100μm, 160μm and SPIRE at 250μm and 350μm. The whole spectral range allow to probe the reprocessed emission coming from dust, and thus could constrain the dust-obscured star-formation processes.

2.2   Sample from Dustpedia

From the large amount of data from Dustpedia, particularly suited for the purposes of the thesis, a modest sample, barely made up of only two galaxies with clear and specific peculiarities, was selected: they both are "grand-design spiral" featured. The main features of NGC3184 and NGC4321 are shown hereafter (Fig. 2.4 - Fig. 2.5).

Galaxy Data

Name: NGC3184
RA(2000): 154.57
DEC(2000): 41.42
Hubble Stage(T): 5.9
Hubble Type: SABc
V (km/s): 592
D25 (arcmin): 7.41
Inclination (deg.): 14.4

Figure 2.4: Galaxy name, coordinates in J2000 system reference, morphological classifications, radial velocity [km/s], D25 size [arcmin] and inclination [°] of the Dustpedia galaxy NGC3184 from the HyperLEDA database (Makarov et al. 2014).

The former is a SABc galaxy (intermediate barred galaxy,less tightly wound spiral arms than (SABa) and somewhat fainter bulge), the latter is a SABb galaxy (intermediate barred galaxy, loosely wound spiral arms, clearly resolved into individual stellar clusters and nebulae; smaller, fainter bulge).

The selection involves galaxies with Hubble stage index T (or RC3) with $2 \leq T \leq 8$ and with diameter $D_{25} > 6'$. The numerical Hubble stage T ranges from - 6 up to + 10: negative
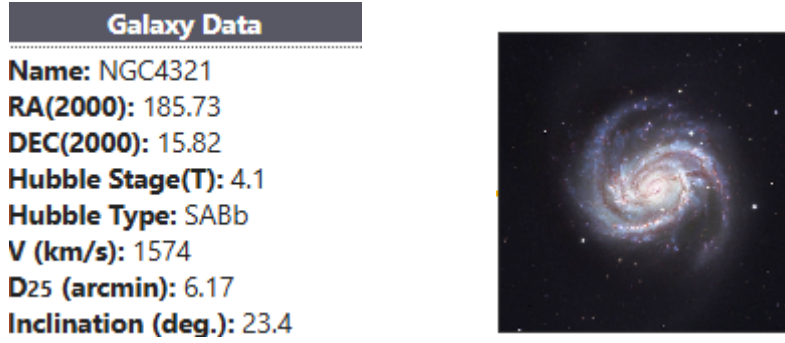
Figure 2.5: Galaxy name, coordinates in J2000 system reference, morphological classifications, radial velocity [km/s], D25 size [arcmin] and inclination [°] of the Dustpedia galaxy NGC4321 from the HyperLEDA database (Makarov et al. 2014).

numbers correspond to early-type galaxies (ellipticals and lenticulars) and positive numbers to late types (spirals and irregulars), thus the sample embraces spirals as above-mentioned (de Vaucouleurs et al. 1991; Corwin et al. 1994), whilst the diameter D_{25} is the semimajor axis of the isophote at which the optical surface brightness (μ_B) falls beneath $25 mag/arcsec^2$.

Being them spiral normal star-forming galaxies, their stellar masses are in the range between $10^{10}M\odot$ - $10^{11}M\odot$ and star formation rates between $1M\odot/yr$ and $4 M\odot/yr$ and these sources represent the evolved descendants of high-redshift normal star-forming galaxies.

Besides the morphological classification, there are three main reasons behind the choice of the selection related to: inclination, distance and photometry.

In order to bypass several problems related to dust correction and/or disk inclination, the two galaxies inclinations *i* lies within 40°, such that they can be said to be nearly face-on galaxies.

Finally, to robustly perform a SED fitting study, the two sources have at least 20 bands of observation upon which it possible to estimate their physical parameters.

In Fig. 2.6 and Fig. 2.7, NGC3184 and NGC4321 are presented as observed in the near and far UV with the GALaxy Evolution eXplorer (GALEX, Morrissey et al. 2007), in the u, r, g, i, z-bands with the Sloan Digital Sky Survey (SDSS, York et al. 2000), in the J, H, K_s-bands with the 2 Micron All-Sky Survey (2MASS, Skrutskie et al. 2006), at 8μm with the Spitzer Space Telescope (Werner et al. 2004), at 3.4μm, 4.6μm, 12μm and 22μm with WISE, at 3.6μm, 4.5μm, 5.8μm, 8.0μm with h the Spitzer Space Telescope (Werner et al. 2004), at 70μm, 100μm, 160μm, 250μm and 350μm and 500 μm with the Herschel Space Observatory (Pilbratt et al.2010).
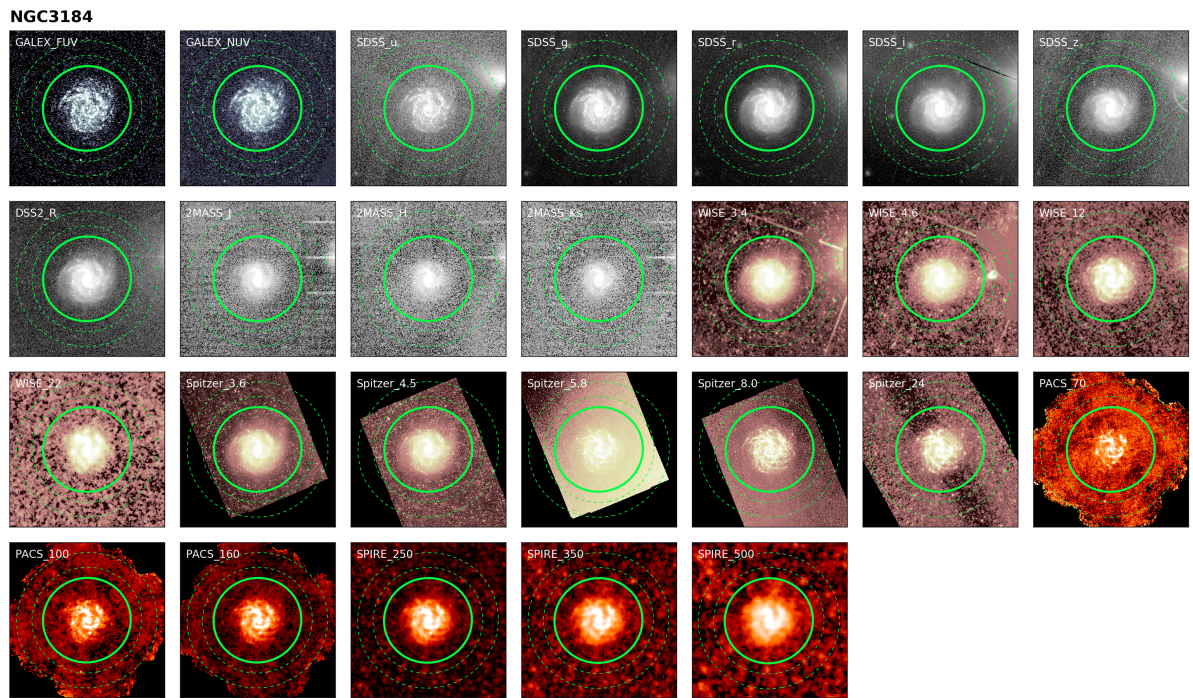
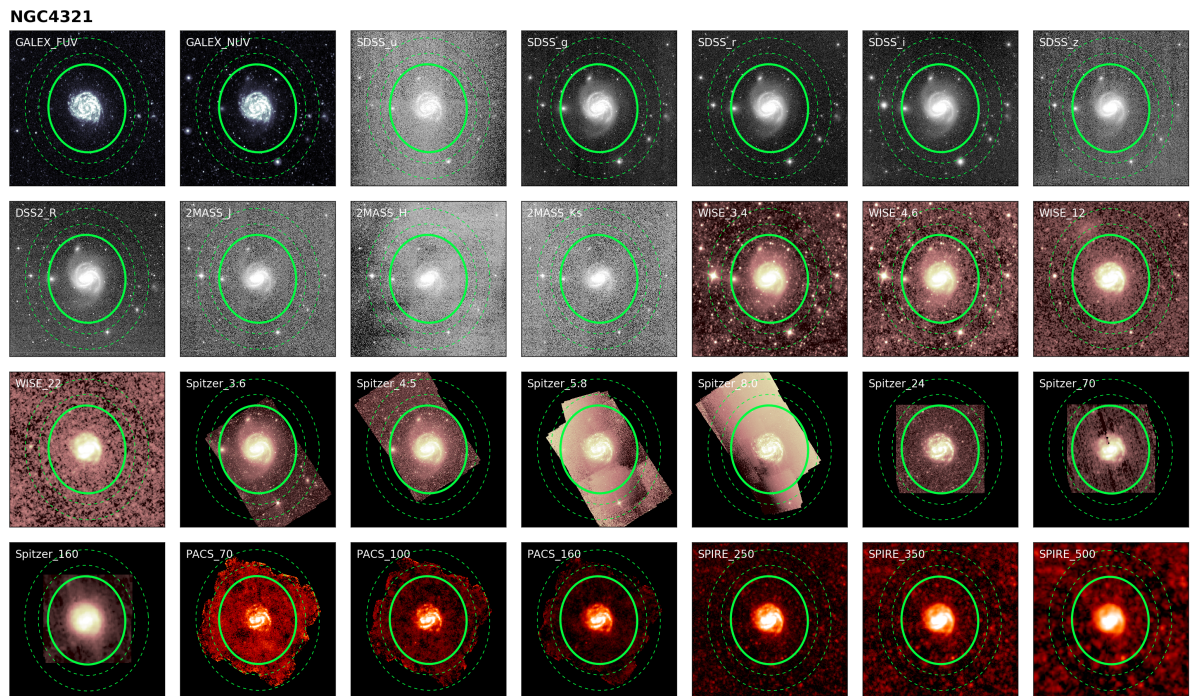Figure 2.6: Multiwavelength imaging available for NGC3184, coming from the DustPedia archive.

NGC4321

Figure 2.7: Multiwavelength imaging available for NGC4321, coming from the DustPedia archive.

Chapter 3

MAGPHYS

The spectral energy distribution (SED) of galaxies provides direct and relevant information about their contents in stars, gas and dust. From the ultraviolet (UV) up to the far-infrared (FIR), every spectral range seems to be a significant tool for the comprehension of galaxy emission. Direct ultraviolet, optical and near-infrared radiations from stars report clear evidence of the past star formation history (SFH); chemical abundances and attenuation due to the presence of dust and a detailed model, which properly describes the emission, will allow to derive statistical estimates of physical parameters such as star formation rate (SFR), stellar mass and dust properties. At wavelengths $\lambda \geq 3\mu m$, the mid- and far-infrared emission reflects the heating of the interstellar medium (ISM) dust by stars of all ages. Extracting constraints on the stellar populations and ISM of galaxies from these multi-wavelength observations implies a rigorous emission model by stars, gas and dust. Currently, the investigation in the mentioned earlier spectral range are widely widespread in the scientific community through GALEX, 2MASS, SDSS, WISE surveys.

To obtain the spatially resolved physical properties of the galaxies examined (stellar mass, $M_\odot$, star formation rate, SFR, for the purpose of the thesis), it is required to perform SED fitting through the publicly available code MAGPHYS (da Cunha et al. 2008). Undoubtedly, there is a necessary strategy to follow which includes: image processing and data reduction, evaluation of the flux after created a grid of cells and the spatially resolved SED fitting.

3.1 SED fitting procedure

3.1.1 Image processing and data reduction

As mentioned in the previous chapter, in order to estimate the spatially resolved physical properties of our interest, it is mandatory to invoke the Dustpedia archive: the database contains different photometric observations (flux maps and error maps in several wavelengths) which need to be downloaded to launch the whole SED fitting analysis. For each photometric map, the reduction process, which combines the background estimation and subtraction and the PSF degradation, has been performed. As regards the former, the procedure follows the indications in Clark et al. (2018) with a sky flattening and then suppression of the background emission. Finally, the background subtracted maps have been degraded to the worst PSF of a band which is assumed to be SPIRE350 ($8''$) which allows not to lose significant pixels. Indeed, the worst PSF is not given by the SPIRE500 band simply because, in this case, the loss of information from the galaxy will start becoming important. To perform the PSF degradation, the maps are convolved using the kernels provided by Aniano et al. (2011) to match each band to the PSF of SPIRE350.

3.1.2 Evaluation of the flux

The second step turns out to be the creation of a grid of coordinates to perform photometry. The reason behind which a grid of cells is built deals with the goal of the project: indeed, a spatially resolved SED-fitting analysis implies to catch the physical properties pixel by pixel. A photometric datum consists in the flux value and in the corresponding error value. In order to measure flux in each band inside the cells, the *photutils v0.6 Python* package (Bradley et al. 2019) has been widely used. On the other hand, the error can be estimated, when available, from the Dustpedia Database. When it is not possible, the signal-to-noise ratio (SNR) of the DustPedia Photometry in that particular band can help to compute the error in each cell. As assumption, the SNR threshold is equal to two: beneath that value, pixels will be ignored for the photometry. Moreover, if a pixel with more than ten bands which the flux measurement cannot be performed in, then the pixel will be rejected. The side of the squared aperture will

be $8''$, the pixel-scale of SPIRE350. As a result, a $8''$ x $8''$ cell catalogue has been produced. The catalogue contains the name and the astrometric positions of the cell centres, the flux values from UV to far-IR and the relative errors.

3.1.3   The spatially resolved SED fitting

Finally, the third and last step involves the SED-fitting procedure which, as previously mentioned, has been performed through the publicly available code MAGPHYS (da Cunha et al. 2008). Before entering into the details of the SED-fitting and analysing the outputs from the code, to provide a better comprehension of the project, a discussion about the description of the MAGPHYS code is required.

3.2   MAGPHYS: a brief description

MAGPHYS - Multi-wavelength Analysis of Galaxy Physical Properties - is a self-contained, user-friendly model package to interpret observed spectral energy distributions of galaxies in terms of galaxy-wide physical parameters related to the stars and the interstellar medium and has been extensively used in the literature.

3.2.1   Stellar emission and attenuation by dust

In a clear Bayesian frame, three detailed models will be discussed to interpret the mid and far-infrared SEDs of galaxies: the spectral evolution of stellar populations, the attenuation by dust and the infrared contribution by stellar clouds. As concerns the first model, the Bruzual & Charlot (2003) population synthesis code was adopted: the stellar populations ages vary between 1 x 10^5 and 2 x 10^{10} yr at a resolution of 3 Å across the whole wavelength range, from 3200 Å to 9500 Å for a wide range of metallicities. This model well reproduces the observed optical and near-infrared colour–magnitude diagrams of Galactic star clusters of various ages and metallicities, initial mass functions (IMFs) and star formation histories. Respecting, instead, the attenuation of starlight performed by dust, the model employed for the purpose is the one by Charlot & Fall (2000): the stellar luminosity is absorbed and then re-emitted, in

the near infrared spectral range, by dust in birth clouds (giant molecular clouds) and in the interstellar medium in galaxies (diffused component). Then, the computed luminosity is distributed in wavelength to give rise to the Spectral Energy Distribution. The remaining model to consider is the infrared emission from the stellar birth clouds, described by the sum of three elements: component of polycyclic aromatic hydrocarbons (PAHs); a mid-infrared continuum characterizing the emission from hot grains at temperatures in the range 130–250 K; and a component of grains in thermal equilibrium with temperature varying in the range $30 - 60$ K. The same three components need to be also considered in the ISM. These are well known and studied in the Milky Way (the so-called cirrus emission) and in order to deal with less variables, for simplicity, they are fixed with an addition of cold grains components with temperature varying in the range $15 - 25$ K.

It is worth briefly analysing the two-component dust model to study the emission of starlight by dust and its passage through the ISM in galaxies. The luminosity per unit wavelength, at time t, from a galaxy, is described as:

$$L_\lambda = \int_0^t dt' \Psi(t - t') S_\lambda(t') e^{-\hat{\tau}_\lambda(t')} \tag{3.1}$$

where Ψ is the star formation rate at time $(t - t')$, $S_\lambda(t')$ is the stellar luminosity per unit mass and wavelength emitted at time t' and $\hat{\tau}_\lambda(t')$ is the effective absorption optical depth of dust at time t'. In particular, the role of dust appears in the effective absorption optical depth: stars are born in dense molecular clouds which tend to dissipate in a time-scale t_o of the order of $\sim 10^7$ yr. Consequently, the stellar emission at time $t' \leq t_o$ is more attenuated than the one provided by older stars. Then:

$$\hat{\tau}_\lambda(t') = \begin{cases} \hat{\tau}_\lambda^{\text{BC}} + \hat{\tau}_\lambda^{\text{ISM}} & \text{for } t' \leq t_o \\ \hat{\tau}_\lambda^{\text{ISM}} & \text{for } t' > t_o \end{cases} \tag{3.2}$$

where $\hat{\tau}_\lambda^{\text{ISM}}$ is the effective absorption optical depth of the interstellar medium and $\hat{\tau}_\lambda^{\text{BC}}$ is the effective optical depth of dust in birth clouds.

The stellar radiation absorbed by dust in the clouds and in the ISM is re-radiated in the infrared and can be defined as the sum of the two components:

$$L_d^{\text{TOT}}(t) = L_d^{\text{BC}}(t) + L_d^{\text{ISM}}(t), \tag{3.3}$$

where $L_d{}^{BC}(t)$ is the total infrared luminosity due to dust in the birth clouds:

$$L_d{}^{BC}(t) = \int_0^{\inf} d\lambda (1 - e^{-\hat{\tau}_\lambda{}^{BC}}) \int_0^{t_0} dt' \Psi(t - t') S_\lambda(t') \tag{3.4}$$

and $L_d{}^{ISM}(t)$ is the total infrared luminosity due to dust in the interstellar medium:

$$L_d{}^{ISM}(t) = \int_0^{\inf} d\lambda (1 - e^{-\hat{\tau}_\lambda{}^{ISM}}) \int_{t_0}^{t} dt' \Psi(t - t') S_\lambda(t') \,. \tag{3.5}$$

3.2.2 Infrared emission of the dust

For the purpose of this project, the strongly interesting point deals with how the stellar emission absorbed and then re-emitted in the infrared is spectrally distributed. As mentioned previously, the study of the Cirrus emission from the Milky Way and from the nearby galaxies allowed us to perform a well-detailed analysis of the several infrared elements to set the frame for the spectral energy distribution. Three are the main components of the infrared emission associated to interstellar dust: PAHs, very small grains and big grains.

- PAHs, polycyclic aromatic hydrocarbons, are strong emission lines mainly arising in the star-forming galaxies at 3.3, 6.2, 7.7, 8.6, 11.3 and 12.7 μm and the Milky Way . They deeply affect the chemistry of the interstellar medium by dominating the photoelectric heating of the gas and controlling the ionization balance: heated up by UV light particles, they emit fluorescent radiation in infrared because of excitation process (Leger & Puget 1984; Allamandola, Tielens & Barker 1985; Leger, D'Hendecourt & Defourneau 1989; Allamandola, Hudgins & Sandford 1999). The probability of a PAH emission is the highest in the so-called "photodissociation regions" on the border between ionized and molecular gas from the H_2 regions where PAH molecules undergo a efficient heating. However, several star-forming galaxies show a component of near-infrared continuum emission characterising the spectral range $3\mu m \leq \lambda \leq 5\mu m$. The origin of these features is still unknown, yet perhaps related to the stochastic heating of PAH molecules (Fig. 3.1).

- very small grains, also known as hot dust ($T_d \simeq 250K$). Even though they have a typical size of the order of $0.01\mu m$, the hot dust constitutes the mid-infrared continuum emission. The component is widely associated to a continuous distribution of small grains which are stochastically heated to high temperatures by the absorption of single UV photons (e.g. Sellgren 1984);
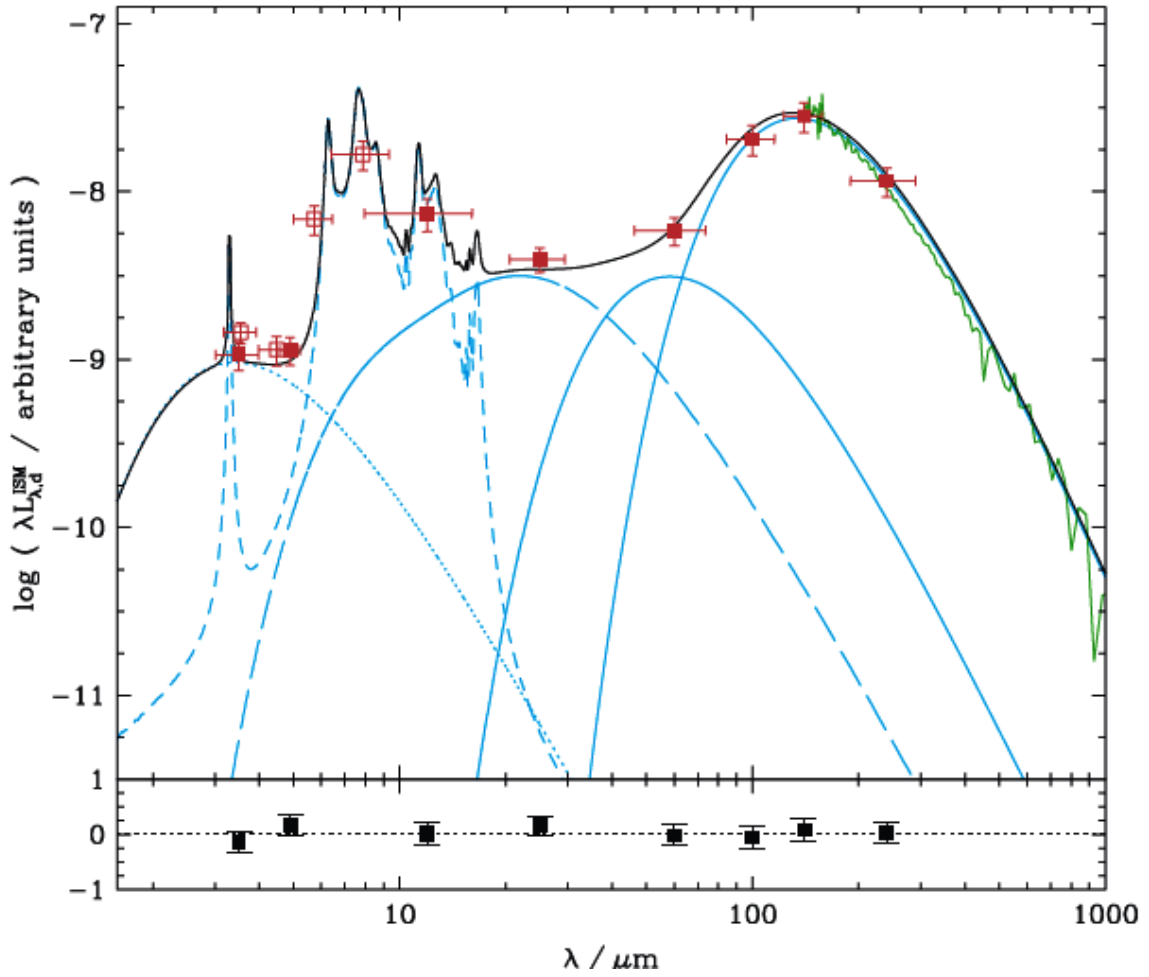
Figure 3.1: In black: best model fit to the observed mean SED of the Galactic cirrus emission. The red filled squares are the COBE/DIRBE observations of Dwek et al. (1997). The Spitzer/IRAC observations of Flagey et al. (2006) are the red open squares and the COBE/FIRAS observations of Dwek et al. (1997) are the green line. Blue lines: the decomposition of the model in its different components: near-infrared continuum (dotted); PAHs (short-dashed); hot mid-infrared continuum (long-dashed) and warm and cold grains in thermal equilibrium (solid).

- big grains leading in the far-infrared domain. In thermal equilibrium with the radiation field at low temperatures and with dimension $0.01\mu m \leq \lambda \leq 0.25\mu m$, the far-infrared SED of a galaxy is a good indicator of dust heating in the ISM. Within the massive dust grains, there are two different types in the model: warm grains with $30K \leq T_{\mathrm{W}} \leq 60K$ and cold grains with $15K \leq T_{\mathrm{C}} \leq 25K$. The former populate both stellar birth clouds and the interstellar medium and the latter only the interstellar medium.

Therefore, in the model, the infrared spectral energy distribution of the birth clouds can be described as:

$$L_{\lambda,\,\mathrm{d}}{}^{\mathrm{BC}} = (\xi_{\mathrm{PAH}}{}^{\mathrm{BC}} l_{\lambda}{}^{\mathrm{PAH}} + \xi_{\mathrm{MIR}}{}^{\mathrm{BC}} l_{\lambda}{}^{\mathrm{MIR}} + \xi_{\mathrm{W}}{}^{\mathrm{BC}} l_{\lambda}{}^{\mathrm{Tw}^{\mathrm{BC}}})(1 - f_{\mu}) L_{d}{}^{tot} \tag{3.6}$$

where $L_{d}{}^{tot}$ is the total infrared luminosity re-radiated by dust and f_{μ} is the fraction of this due to the interstellar medium, $l_{\lambda}{}^{\mathrm{PAH}}$, $l_{\lambda}{}^{\mathrm{MIR}}$, $l_{\lambda}{}^{\mathrm{Tw}^{\mathrm{BC}}}$ are respectively the spectral energy distribution associated to PAHs, the hot mid-infrared continuum emission and the warm far-infrared emission in thermal equilibrium with:

$$\xi_{\mathrm{PAH}}{}^{\mathrm{BC}} + \xi_{\mathrm{MIR}}{}^{\mathrm{BC}} + \xi_{\mathrm{W}}{}^{\mathrm{BC}} = 1 \tag{3.7}$$

where $\xi_{\mathrm{PAH}}{}^{\mathrm{BC}}, \xi_{\mathrm{MIR}}{}^{\mathrm{BC}}, \xi_{\mathrm{W}}{}^{\mathrm{BC}}$ are the relative infrared luminosity contributions from PAHs, the mid-infrared domain and the warm dust to birth clouds.

Whereas, equivalently, the infrared spectral energy distribution of the surrounding interstellar medium will be satisfied by:

$$L_{\lambda,\,\mathrm{d}}{}^{\mathrm{ISM}} = (\xi_{\mathrm{PAH}}{}^{\mathrm{ISM}} l_{\lambda}{}^{\mathrm{PAH}} + \xi_{\mathrm{MIR}}{}^{\mathrm{ISM}} l_{\lambda}{}^{\mathrm{MIR}} + \xi_{\mathrm{W}}{}^{\mathrm{ISM}} l_{\lambda}{}^{\mathrm{Tw}^{\mathrm{ISM}}} + \xi_{\mathrm{C}}{}^{\mathrm{ISM}} l_{\lambda}{}^{\mathrm{Tc}^{\mathrm{ISM}}})(f_{\mu} L_{d}{}^{tot}) \tag{3.8}$$

with

$$\xi_{\mathrm{PAH}}{}^{\mathrm{ISM}} + \xi_{\mathrm{MIR}}{}^{\mathrm{ISM}} + \xi_{\mathrm{W}}{}^{\mathrm{ISM}} + \xi_{\mathrm{C}}{}^{\mathrm{ISM}} = 1 \tag{3.9}$$

where $\xi_{\mathrm{PAH}}{}^{\mathrm{ISM}}, \xi_{\mathrm{MIR}}{}^{\mathrm{ISM}} \xi_{\mathrm{W}}{}^{\mathrm{ISM}}, \xi_{\mathrm{C}}{}^{\mathrm{ISM}}$ are the relative infrared luminosity contributions from PAHs, the mid-infrared domain, the warm and the cold grains to the interstellar medium. Concerning the $\xi_{\mathrm{MIR}}{}^{\mathrm{ISM}}$, it can be treated as constant: the intensity of the average radiation field heating dust in the interstellar medium of normal galaxies is roughly the same. To support the hypothesis, it is suitable to address the observations of high Galactic latitude (cirrus) dust emission in

the Milky Way to constrain the mid-infrared SED parameter of the ISM. That is significantly convenient from a computational point of view for the model: the reduction of variables will undoubtedly improve the coding.

In conclusion, for a complete and proper description of the model, it is helpful to relate the global contribution of a distinct dust component (PAHs, the hot mid-infrared continuum and warm and cold dust) to the total infrared luminosity of a general galaxy (in thermal equilibrium) both in birth clouds and in the ambient interstellar medium (Fig. 3.2):
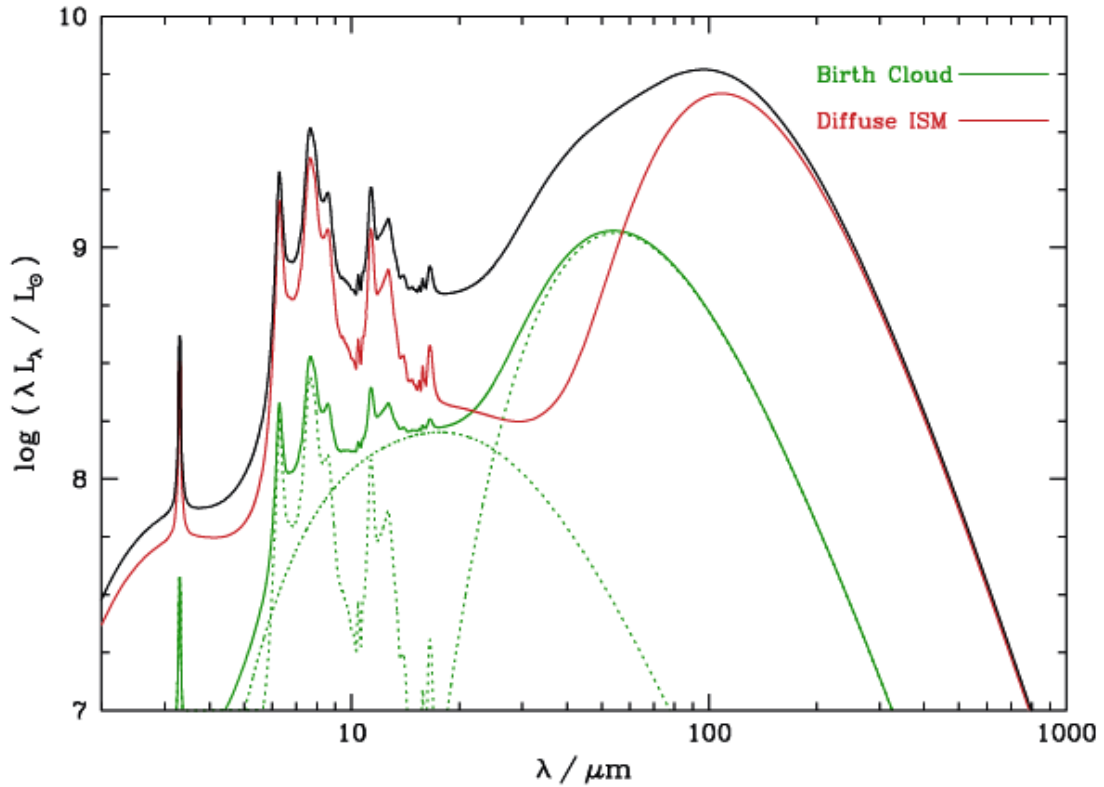
Figure 3.2: Example of infrared spectral energy distribution computed using the model presented in Section 1.2, for 'standard' values of the parameters: $f\mu$ = 0.6, ξ_{PAH}^{BC} = 0.05, ξ_{MIR}^{BC} = 0.15, ξ_W^{BC} = 0.80, T_W^{BC} = 48 K, ξ_C^{ISM} = 0.8 and T_C^{ISM} = 22 K. Black curve: total infrared spectrum. Green solid curve: contribution by dust in the stellar birth clouds and the green dashed curves show the breakdown of this contribution in different components: PAHs, hot mid-infrared continuum and warm dust in thermal equilibrium. Red curve:contribution by dust in the ambient ISM.

$$\xi_{\text{PAH}}{}^{\text{tot}} = \xi_{\text{PAH}}{}^{\text{BC}}(1 - f_\mu) + 0.550(1 - \xi_{\text{C}}{}^{\text{ISM}})f_\mu, \tag{3.10}$$

$$\xi_{\text{MIR}}{}^{\text{tot}} = \xi_{\text{MIR}}{}^{\text{BC}}(1 - f_\mu) + 0.275(1 - \xi_{\text{C}}{}^{\text{ISM}})f_\mu, \tag{3.11}$$

$$\xi_{\text{W}}{}^{\text{tot}} = \xi_{\text{W}}{}^{\text{BC}}(1 - f_\mu) + 0.175(1 - \xi_{\text{C}}{}^{\text{ISM}})f_\mu, \tag{3.12}$$

$$\xi_{\text{C}}{}^{\text{tot}} = \xi_{\text{C}}{}^{\text{ISM}}f_\mu. \tag{3.13}$$

3.2.3   SED-fitting

MAGPHYS exploits the so-called "energy balance" principle: it simultaneously models the emission observed in the whole spectral range (from UV to far-IR) through the assumption that the energy output is balanced between the one in UV/optical/near-IR wavelengths which is absorbed by dust and the one re-emitted in the mid-IR and far-IR. The fitting process takes the advantage of a purely Bayesian approach adopted in order to figure out the posterior distribution functions of the parameters by fitting the previously processed photometry to the model emission directly coming from the MAGPHYS libraries formed by 50000 stellar population spectra with different star formation histories described by a continuous declining model:

$$\Psi(t) \propto \exp^{-\gamma\,t} \tag{3.14}$$

The libraries involve a set of uniformly distributed physical parameters: formation age ranges between 0.1 Gyr and 13.5 Gyr (shorter or equal to the age of the Universe), the star formation timescale varies between 0 Gyr^{-1} and 0.6 Gyr^{-1} with a characteristically drop (directly due to the declining model assumed for the star formation history) at 1 Gyr^{-1} and metallicity fluctuates between 0.02 $Z_\odot$ and 2 $Z_\odot$.

Finally, the criterion chosen to accept or reject a fit is the χ^2 threshold: for $\chi^2 > 25$, the fit is automatically rejected.

SED-fitting outputs: stellar mass and SFR

$M_\star$ values are directly given as a MAGPHYS output, whilst SFR values are obtained as:

$$SFR = SFR_{UV} + SFR_{IR} \tag{3.15}$$

where the ultraviolet SFR, $SFR_{\rm UV}$, gives the unobscured component of the star formation rate and the infrared star formation rate, $SFR_{\rm IR}$, the obscured component. SFRs are not taken as a direct MAGPHYS output because, in that case, the value would be more dependent on degenerate parameters like extinction, age and metallicity. In particular,

$$SFR_{UV} = 0.88 x 10^-28 L_\nu \qquad (3.16)$$

with L_ν in *erg s^{-1} Hz^{-1}* is the luminosity per unit frequency evaluated at 150μm (from Bell & Kennicutt, 2001) whereas

$$SFR_{IR} = 2.64 x 10^-44 L_{IR} \qquad (3.17)$$

with $L_{\rm IR}$ in *erg s^{-1}* is the luminosity evaluated from the SED fit between 8μm and 1000μm (from Kennicutt, 1998).

For each source, it was possible to plot the maps of stellar mass, star formation rate, the distribution of the cells in the $\log\Sigma_\star$-$\log\Sigma_{\rm SFR}$ plane (i.e. the Main Sequence) and distance from the MS (Fig. 3.3 - 3.10).

As outputs from the MAGPHYS code, each aperture of the galaxy examined is equipped with astrometric coordinates (RA[deg] and DEC[deg]) which were used in the first three plots and combined with $\Sigma_\star$ and $\Sigma_{\rm SFR}$, respectively stellar mass density and SFR density.

The two were obtained by simply dividing the $M_\odot$ and SFR quantities with the area given by the square of the side aperture. The reason behind the choice of stellar mass density and SFR density rather than usual stellar mass and SFR values is the opportunity to compare the plots with other galaxies plots. It is very clear that the stellar mass distribution is fainter in the whole galaxy with the exception of the centre where the mass is significantly condensed. As concerns the SFR, the distribution picks in the centre and along the spiral arms, therefore the SFR traces the spiral pattern of the galaxies.

The two remaining plots both focus on the Main Sequence (MS) described as the spatially resolved relation between $M_\odot$ and $\Sigma_{\rm SFR}$. Considering all the accepted ($\chi^2 < 25$) cells coming from eight galaxies (with NGC3184 and NGC4321 among them) in the $\log\Sigma_\star$-$\log\Sigma_{\rm SFR}$ plane, Enia et al. (2020) performed the fit to compute the MS relation using EMCEE (Foreman-Mackey et al. 2013). The fit, a log-linear relation, described as:

$$\log\Sigma_{\rm SFR} = m\,\log\Sigma_\star + q \qquad (3.18)$$

gave the following results:

$$m = 0.82 \pm 0.12 \tag{3.19}$$

and

$$q = -8.69 \pm 0.97 \tag{3.20}$$

The figure shows the distribution of the data around the MS in function of the distance of each cell from the galaxy centre.

Finally, the last figure shows the distance of each cell from the MS, Δ_{MS}, given as the perpendicular distance of a point in the $\log \Sigma_\star$-$\log \Sigma_{\mathrm{SFR}}$ plane from the MS relation. It is evident that for the NGC3184, the central bulge is less star-forming than the spiral arms, however, for the NGC4321 the opposite is true. It is worth pointing out that, the galaxy has got a very remarkable "quenched ring": the portion of NGC4321 (at the lowest stellar mass densities, i.e. at large galactocentric distances) clearly lying underneath the MS, suppressed star formation and seems not to "approach" the spiral arms. It is still to be understood if this low SFR outer part of the galaxy is associated to an older population migrated out of the disk or if it is the remnant of external accretion through merging (See Chapter 3).
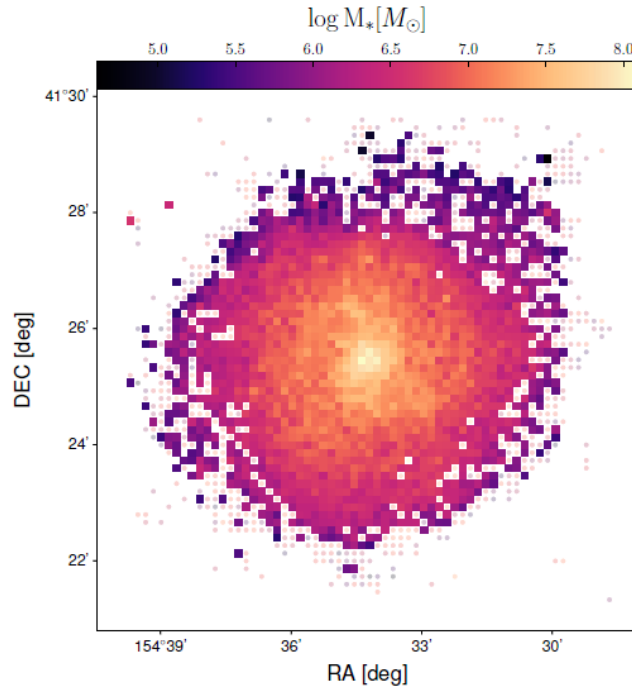
Figure 3.3: NGC3184: cells log stellar mass. The cell rejected (over the threshold) are showed as points.
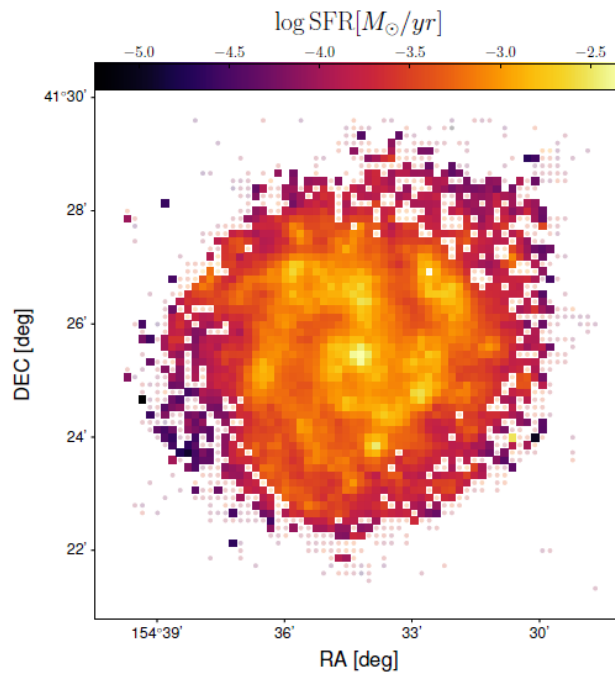

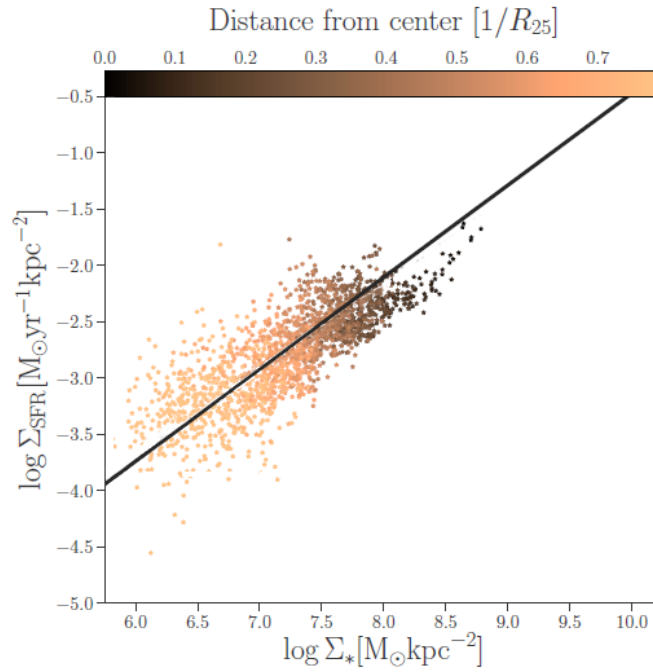Figure 3.4: NGC3184: cells log star formation rate. The cell rejected are showed as points.

Figure 3.5: NGC3184: $\log \Sigma_\star$-$\log \Sigma_{\mathrm{SFR}}$ plane. Cells are color-coded according to the distance from the galaxy center in units of r25. The black solid line is the MS.
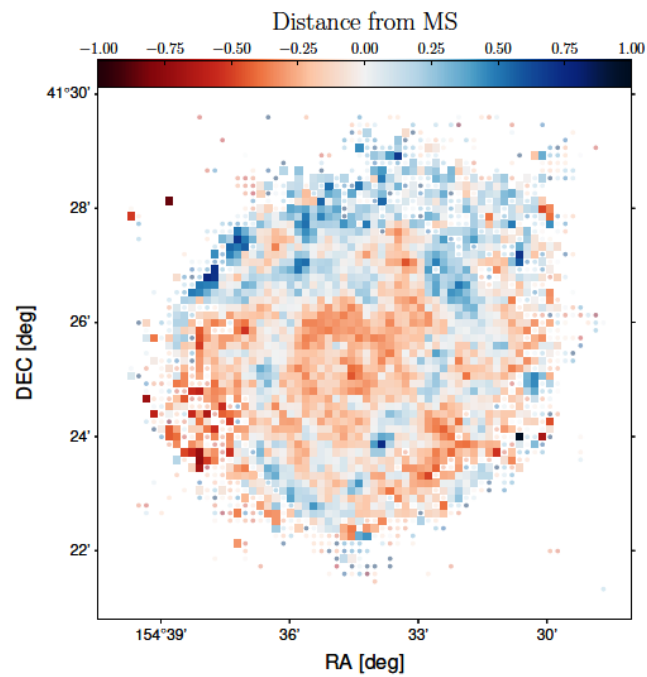

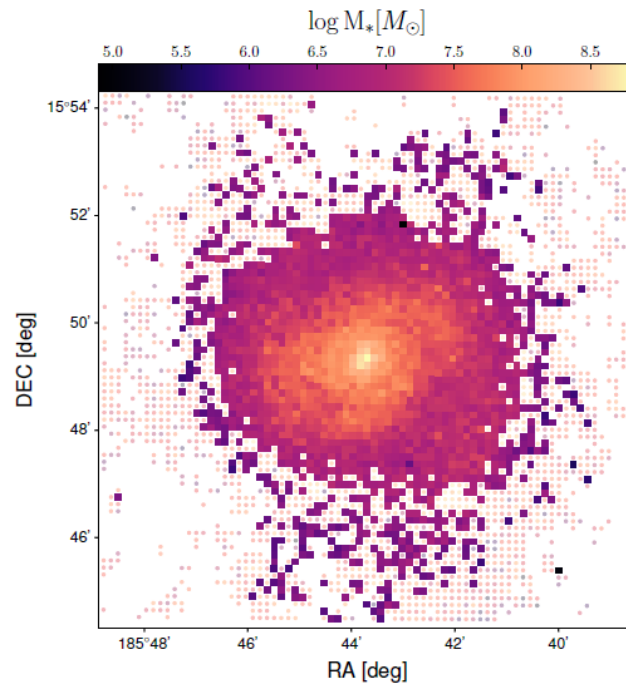Figure 3.6: NGC3184: cell distance from the MS.

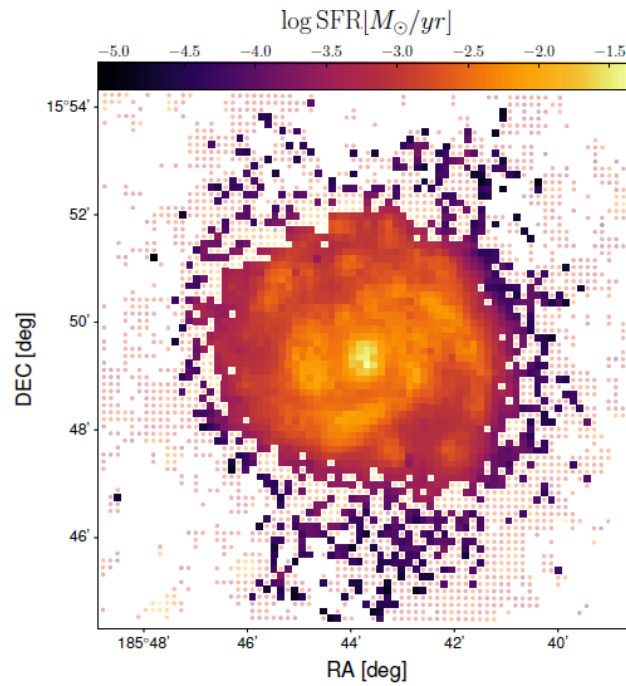Figure 3.7: NGC4321: cells log stellar mass. The cell rejected are showed as points.

Figure 3.8: NGC4321: cells log star formation rate. The cell rejected are showed as points.
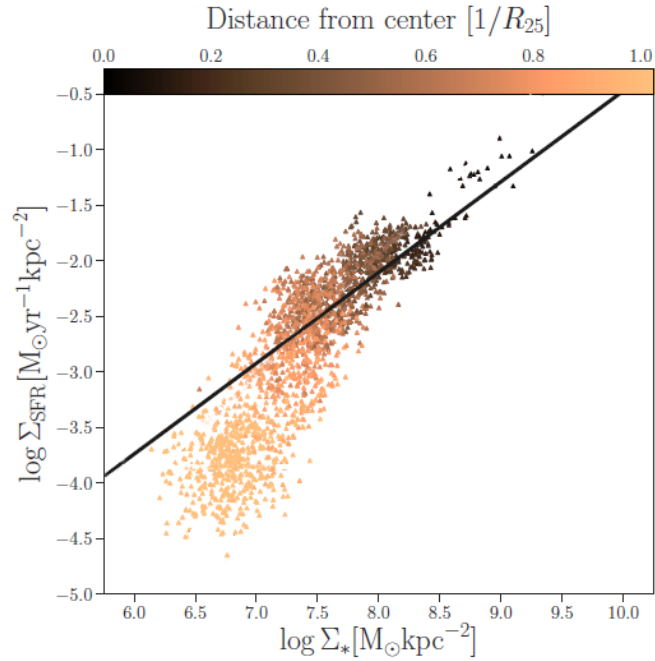
Figure 3.9: NGC4321: $\log \Sigma_\star$-$\log \Sigma_{\rm SFR}$ plane. Cells are color-coded according to the distance from the galaxy center in units of r25. The black solid line is the MS.
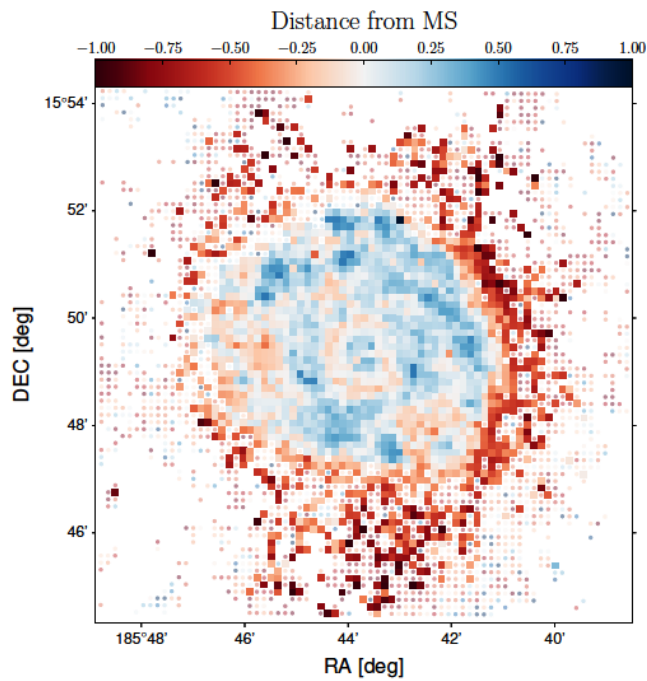

Figure 3.10: NGC4321: cell distance from the MS.

Chapter 4

BAGPIPES

For the purpose of the thesis, a further explored investigation on the star formation history (SFH) of the galaxies examined is highly required. However, the MAGPHYS project, as previously discussed, does not allow the user to obtain SFH as an output from the code; indeed, SFH model is provided as "fixed" quantity which, clearly, cannot be parametrized and chosen in relation to the available data. That is the main reason behind which another and recent code has been largely used in this thesis project. The structure of the next chapters is as follows: in this one, the SFH parameters and the remaining quantities (stellar mass, SFR) will be discussed as outputs from the BAGPIPES code; the next one, instead, will be devoted to a brief comparison between the two codes: MAGPHYS and BAGPIPES.

Two are the main factors which supported the creation of the code: rapid advances in the availability of studies of galaxy evolution and the increasingly development of new Bayesian technique such as Markov chain Monte Carlo, MCMC, (Goodman & Weare 2010; Foreman-Mackey et al. 2013) and nested sampling algorithms (Skilling 2006, Feroz & Hobson 2008; Feroz et al. 2009, 2013). In particular, progresses in near-infrared capability of both spectroscopic and photometric instruments and the brand new techniques employed for multi-object and integral-field spectrographs allowed the scientific community to study on larger size samples. However, that is not all. To obtain constraints on the parameters of interest, the Bayesian approach calls for a model of the light emitted by the source distributed in wavelengths (i.e. spectral energy distribution, SED) which has to be fitted with the observed SED in order to derive the posterior distribution for the model parameters and hence marginalize the so-called

nuissance parameters. The combination of the rising quality and quantity of data and new statistical techniques set the perfect frame for BAGPIPES.

Written in the Python programming language and in a evident Bayesian framework, Bayesian Analysis of Galaxies for Physical Inference and Parameter EStimation, also known as BAGPIPES, is a spectral fitting code, designed both to model the emission from galaxies from the far-ultraviolet to the microwave spectral range and to fit these models to arbitrary combinations of spectroscopic and photometric observational data using the MultiNest nested sampling algorithm (Feroz & Hobson 2008; Feroz et al. 2009, 2013).

Before entering into the details of the code, to clarify, times *t* are measured forwards from the beginning of the Universe (*t(z)* is the age of the Universe at redshift *z*), whereas *a* are ages, which are measured backwards in time (*t(z_{obs})* is the age from the observed redshift).

Finally, the cosmological constant used are:

$$\Omega_{\mathrm{M}} = 0.3,\ \Omega_{\Lambda} = 0.7,\ H_0 = 70 km s^{-1} Mpc^{-1}. \tag{4.1}$$

4.1 The BAGPIPES code

4.1.1 Galaxy spectra model generation

A real distinctive aspect of BAGPIPES is the generation of physically realistic model for galaxy spectra in a wide range: from the far-ultraviolet up to the microwave regime. A very large amount of quantity can be recovered from it: spectral data in the desired wavelength range, photometric fluxes through previously-specified filters and emission-line fluxes. Plots show the luminosity per unit rest-frame wavelength, $L_\lambda(\lambda)$, as a function of λ. The wavelength along the x-axis is reproduced thanks to the filter the user had to define from the filter source recommended "SVO Filter Profile Service". To construct, instead, the luminosity, there are four different factors that need to be included:

$$L_\lambda(\lambda) = \sum_{j=1}^{N_{\mathrm{C}}} \sum_{i=1}^{N_{\mathrm{a}}} SFR_{\mathrm{j}}(t_{\mathrm{i}}) SSP(a_i, \lambda, Z_j) T^+(a_i, \lambda) T^0(a_i, \lambda) \Delta_{\mathrm{a_i}} \tag{4.2}$$

where SFR(t), the star formation history, SSP, simple stellar-population models (which are in function of *a*,the age of stellar population, λ, the wavelength and *Z*, the stellar metallicity and the initial mass function, IMF), T^+, the transmission function of the ionized ISM and T^0, the transmission function of the neutral ISM are the four main elements to build up the luminosity in the model. All of these will be individually analyzed in the following sections. Moreover, *i* runs across the age bins and Δ_i is the width of these bins, *j* runs across SFH components, N_c is the number of SFH components and N_a the number of age bins. As mentioned before:

$$t_i = t(z_{obs}) - a_i \tag{4.3}$$

Once known the luminosity, it is convenient to set the observed frame in order to determine the flux density in the observed frame. To proceed this way, it is helpful to recall how to compute the observed wavelength

$$\lambda_{obs} = (1 + z_{obs})\lambda \tag{4.4}$$

to recover the observed frame flux density $(f_{\lambda_{obs}})(\lambda_{obs})$

$$f_{\lambda_{obs}}(\lambda_{obs}) = \frac{L_\lambda(\lambda)}{4\pi D_L(z_{obs}^2)(1 + z_{obs})} T_{IGM}(\lambda, z_{obs}) \tag{4.5}$$

where $L_\lambda(\lambda)$ is the already discussed luminosity, D_L is the redshifted luminosity distance and $T_{IGM}(\lambda, z_{obs})$ is the transmission function of the intergalactic medium, whose attenuation model, provided by Inoue et al. (2014), was integrated in the BAGPIPES code.

Stellar population synthesis

The pre-defined Stellar Population Synthesis (SPS) models, implemented in the code, are the 2016 version of the (see section 2.3.1) Bruzual & Charlot (2003) models of different ages across a range of metallicities.

Star-formation histories

The star-formation history, in BAGPIPES, is obtained as the sum of all the unlimited number of j-components with a defined expression for the star-formation rate as a function of time, $SFR_j(t)$. The availability of individual function form for the SFH is remarkable and includes:

-Delta function,

-Constant,

-Exponentially declining,

-Delayed exponentially declining,

-Log-normal,

-Double-power-law.

For the purpose of the thesis and the sample considered, the Delayed exponentially declining model, enriched by a burst component, was the most suitable. Therefore,

$$SFR(t) = \sum_{j=1}^{N_c} SFR_j(t). \tag{4.6}$$

The $SFR_j(t)$ are computed for all times t_i

$$t_i = t(z_{obs}) - a_i, \tag{4.7}$$

then, $SFR_j(t_i)$ is set to zero when, since the age of the stellar population, a_i, is less than the age of the Universe at observed redshift, z_{obs}, all t_i are greater than the age of the Universe. Furthermore, each component requires a total mass of star formed, M_{formed} and a metallicity value Z_j, to be specified in the model.

Nebular emission

The nebular-emission model is constructed from Byler et al. (2017): the nebular-emission from a galaxy is assumed to be the sum of emission from different ages H_{II} regions which are modeled with a spherical shell geometry and fixed radius. The model is refined with the Solar abundances of Anders & Grevesse (1989) and the metallicity of the ionized gas is supposed to be the same as the stars producing ionizing photons. Through the latest version (2017) of the CLOUDY code which reproduces the observed extinction properties of the ISM in the Milky Way, it was possible to include dust grains in BAGPIPES.

Dust attenuation and emission

Each attenuation curves in BAGPIPES takes the comprehensive form:

$$log_{10}(T^0(a_i, \lambda)) = \begin{cases} -\frac{0.4\epsilon A_V k(\lambda)}{R_V} & a_i < a_{BC} \\ -\frac{0.4 A_V k(\lambda)}{R_V} & a_i > a_{BC} \end{cases} \tag{4.8}$$

where ϵ is a constant used to control the extra attenuation towards H_{II}, A_V is the attenuation in magnitude in the V-band (5500 Å), $k(\lambda)$ and R_V are related to the dust model chosen and a_{BC} is the lifetime of stellar birth clouds. The dust model implemented in BAGPIPES is the Calzetti et al. (2000) extinction law because of the local star-forming galaxies in the sample.

The extinction at a wavelength λ is related through the color excess $E(B-V)$ and to the reddening curve $k(\lambda)$:

$$A_\lambda = k(\lambda)E(B\text{-}V) = \frac{k(\lambda)A_V}{R_V} \tag{4.9}$$

with $R_V = 4.05 \pm 0.80$ and

$$k(\lambda) = \begin{cases} 2.659(-2.156 + \frac{1.509}{\lambda} - \frac{0.198}{\lambda^2 + \frac{0.011}{\lambda^3}}) + R_V & 0.12\mu m \leq \lambda \leq 0.63\mu m \\ 2.659(-1.857 + \frac{1.040}{\lambda}) + R_V & 0.63\mu m \leq \lambda \leq 2.20\mu m \end{cases} \tag{4.10}$$

For shorter wavelengths (i. e. in the near-ultraviolet), $k(\lambda)$ and R_V are extrapolated through a power-law fit to the dust curve.

Instead, as concerns the dust emission, it is modelled by two separate components: the hot dust component (from the CLOUDY output) accounting for the H_{II} regions and the greybody component for the cold dust.

4.1.2 Model fitting

One of the reason behind the choice of the BAGPIPES code for this project is its ability and rapidity of fitting the observational data in a pure Bayesian framework. The fitted data (Fig. 4.1 - Fig. 4.2)were already widely described in Chapter 3 since they are photometry point outputs coming from the MAGPHYS code (flux computed in each wavelength and the relative error). It is worth giving a brief description of the Bayesian inference methodology.

Bayesian inference methodology

Bayesian inference is an important technique in statistics in which Bayes' theorem is used to update the probability for a hypothesis as more information is added and becomes available. Consider parameter space and then parameter vector, Θ, a hypothesis, H and new data, D, the Bayes' theorem asserts that:

$$P(\Theta|D, H) = \frac{P(D|\Theta, H)P(\Theta|H)}{P(D|H)} \tag{4.11}$$

where $P(D|\Theta, H)$ is the probability of obtaining data given the hypothesis and the parameter vector. It is the so-called *likelihood*, $L(D|\Theta, H)$. $P(\Theta|H)$ describes the probability of having the parameter vector given the hypothesis; the so-called prior probability that is to say the probability of what is already known. Finally, the $P(D|H)$ is the evidence which is the probability of having the data given the hyphotesis and $P(\Theta|D, H)$ is the posterior distribution, i.e. the probability once the new data are considered.

In the case of BAGPIPES code, the hypothesis consists of a specific model parameterisation (i.e. dust model, type of SFH components etc.) and once the hypothesis is constructed, the prior probability distributions for the model parameters can be defined to provide observational data. f_i (for the purpose of the thesis, only photometric data are fitted) and the corresponding uncertainties, σ_i to constraints those parameters. When a parameter is fitted, it is mandatory to specify an upper and lower limit on the parameter value and form for the prior probability density between these limits. In BAGPIPES, it is possible to specify the parameter prior distribution or pick from a number of options offered to the user.

As regards, instead, the likelihood function, it is assumed that uncertainties are Gaussian distributed and independent, such that the log-likelihood can be written as:

$$\ln(L) = -0.5 \sum_i \ln(2\pi\sigma^2) - 0.5 \sum_i \frac{(f_i - f_i^H(\Theta))^2}{\sigma_i^2} \tag{4.12}$$

where f_i^H is the model prediction to the observed flux f_i.

To determine posterior distribution and evidence quantity starting from prior distribution, and observational data available, BAGPIPES widely makes use of MultiNest (Feroz & Hobson 2008; Feroz et al. 2009, 2013), accessed through the PyMultiNest interface (Buchner et al. 2014). Then, once the posterior distribution is provided by MultiNest, BAGPIPES processes

it to finally obtain information of our interest: posterior spectrum and SFH plots (Fig. 4.3 - 4.6) with samples for the fitted parameters from the posterior distribution (Table 4.1): age, mass formed, metallicity, tau, A_V, stellar mass, SFR, nSFR, sSFR, mass weighted age, time of formation and SFH. Stellar mass, SFR, main sequence distance plots are shown in Fig 4.7 - Fig. 4.14.
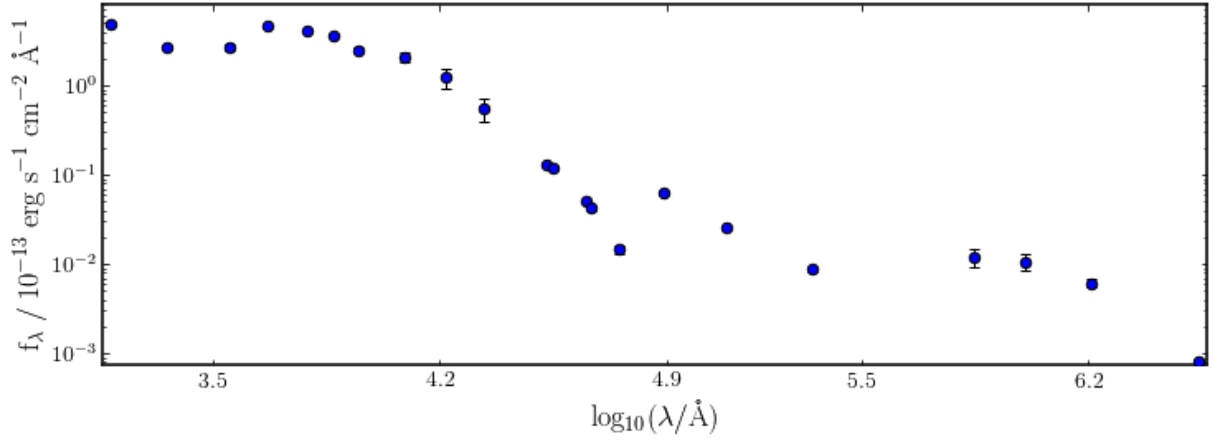
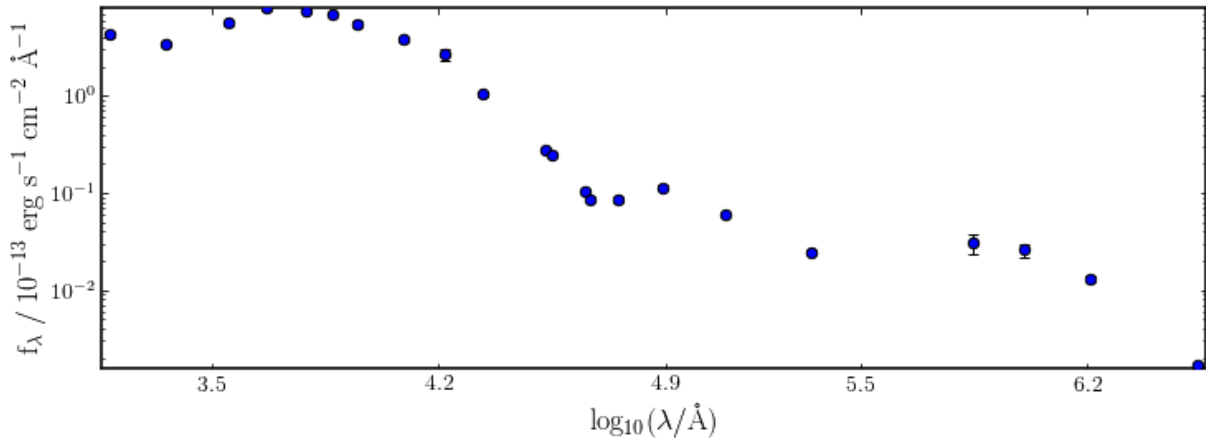Figure 4.1: NGC3184: spectral energy distribution with photometric data from the MAGPHYS code.

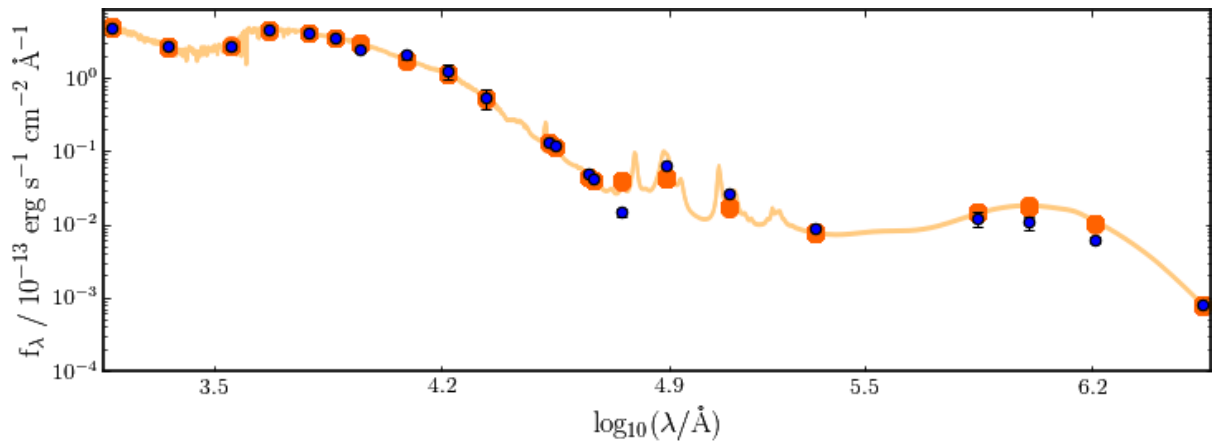Figure 4.2: NGC4321: spectral energy distribution with photometric data from the MAGPHYS code.

Figure 4.3: NGC3184: the photometry from the MAGPHYS code is shown in blue. The 16th to 84th percentile range for the posterior spectrum and photometry are shaded orange.
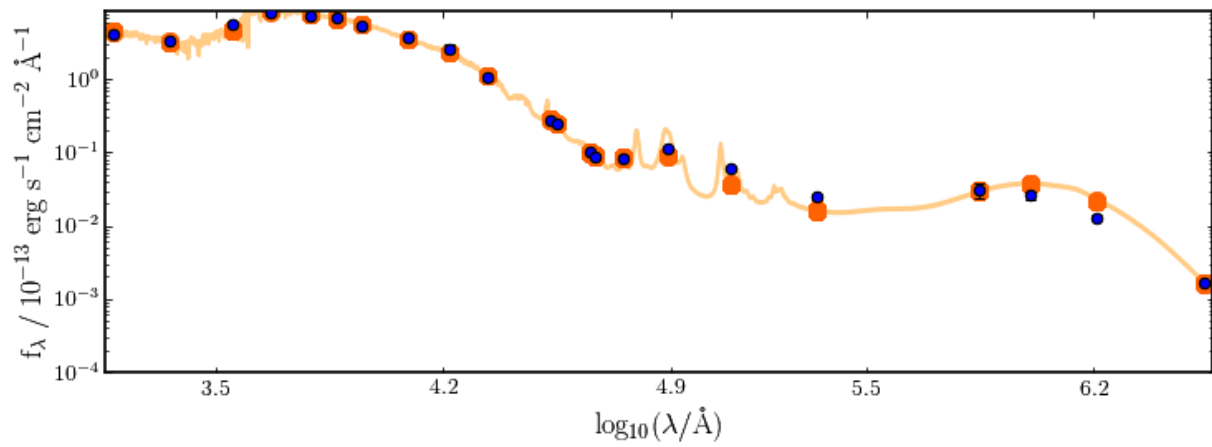

Figure 4.4: NGC4321: the photometry from the MAGPHYS code is shown in blue. The 16th to 84th percentile range for the posterior spectrum and photometry are shaded orange.
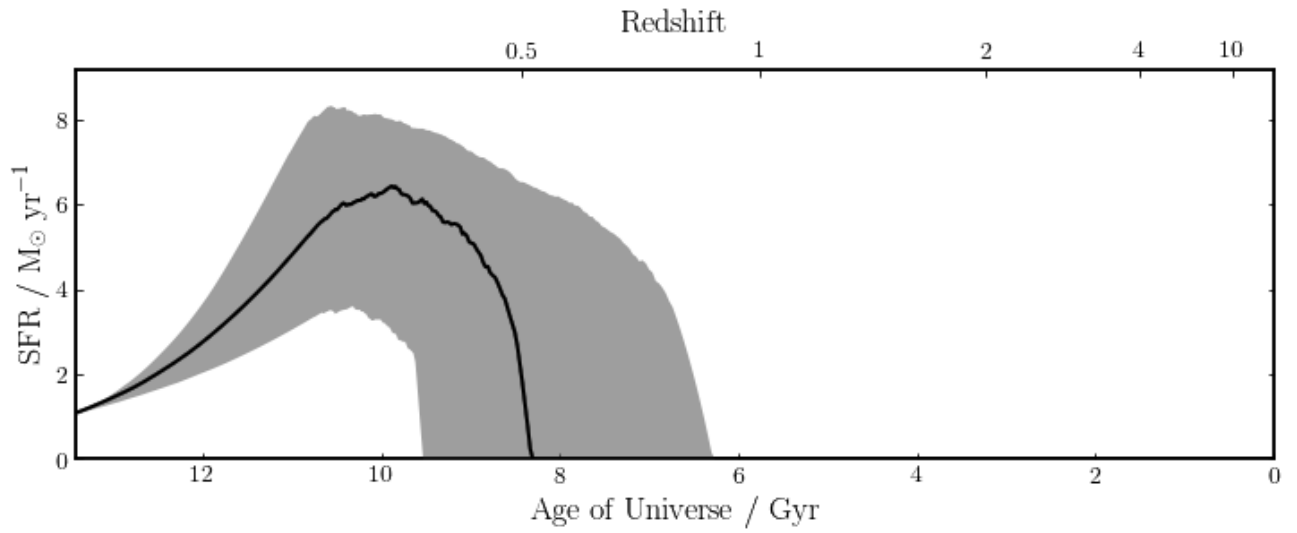
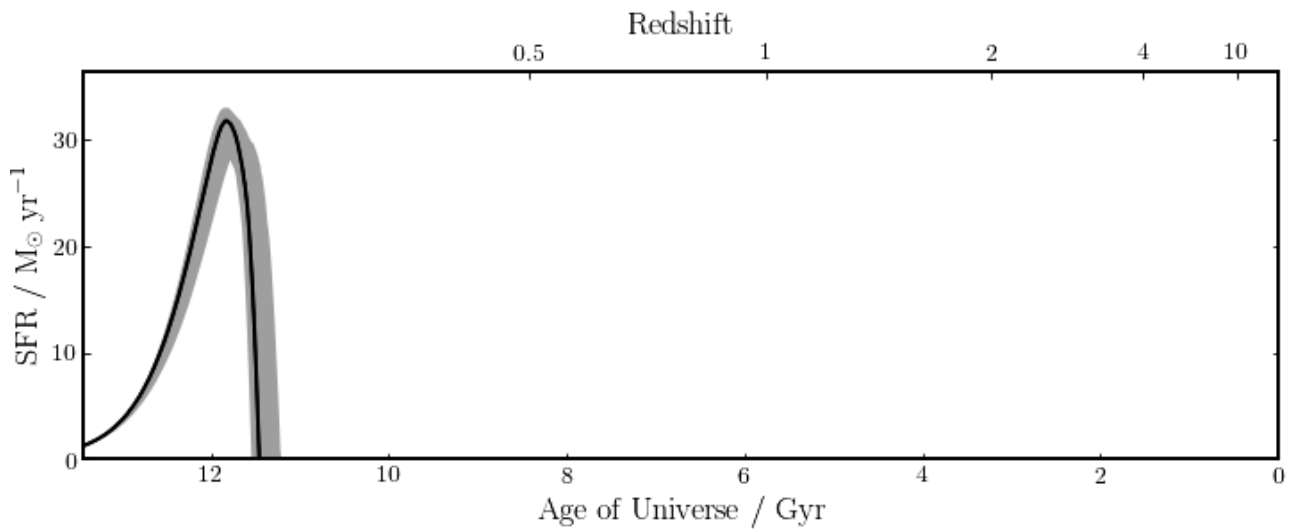Figure 4.5: NGC3184: posterior Star Formation History information

Figure 4.6: NGC4321: posterior Star Formation History information

Burst: age	0.057 Gyr
Burst: mass formed	3.62 M$\odot$
Burst: metallicity	1.19 Z$\odot$
Delayed: age	5.11 Gyr
Delayed: mass formed	10.36 M$\odot$
Delayed: metallicity	0.24 Z$\odot$
Delayed: tau	1.14 Gyr
Dust: Av	0.4 mag
stellar mass	10.07 M$\odot$
formed mass	10.36 M$\odot$
SFR	1.13 M$\odot$/yr
sSFR	-10.01 M$\odot$/yr/M$\odot$
nSFR	-0.18 M$\odot$/yr Mpc^{-3}
Mass weighted age	3.11 Gyr
t form	10.32 Gyr
t quench	99 Gyr
SFH	1.13 M$\odot$/yr

Table 4.1: Samples from the posterior distribution for NGC3184

Burst: age	0.06 Gyr
Burst: mass formed	3.7 M$\odot$
Burst: metallicity	1.23 mag
Delayed: age	1.97 Gyr
Delayed: mass formed	10.45 M$\odot$
Delayed: metallicity	0.25 mag
Delayed: tau	0.33 Gyr
Dust: Av	0.56 mag
stellar mass	10.2 M$\odot$
formed mass	10.45 M$\odot$
SFR	1.48 M$\odot$/yr
sSFR	-10.04 M$\odot$/yr/ M$\odot$
nSFR	-0.16 M$\odot$/yr Mpc^{-3}
Mass weighted age	1.34 Gyr
t form	12.08 Gyr
t quench	99 Gyr
SFH	1.37 M$\odot$/yr

Table 4.2: Samples from the posterior distribution for NGC4321

4.2 Star-Formation history models

There are three types of possible model for galaxy star-formation histories (SFHs): parametric, non-parametric models and models drawn directly from simulations. There is still much debate in the literature about the best approach to use: the parametric one requires to impose strong priors on physical parameters; indeed, measurements of the galaxy stellar-mass function, star-formation rate density (SFRD) and star-forming main sequence (SFMS) can be significantly biased. On the other hand, the non-parametric model allows a noteworthy flexibility with few constraints on the prior assumptions. However, the speed and simplicity of fitting of the parametric model make them widely widespread in the scientific community. Improvements in the flexibility of modeling SFHs have been made by using more complex parameterisations, at the expense of computational tractability.

For the scope of this project, the idea is, just to start, to obtain physical properties of the sample considered by adopting a "parametric" approach and then, in future works, the intent is to compare the outputs from parametric models with the results from non-parametric models. By using the BAGPIPES code, NGC3184 and NGC4321 will be explored through the delayed exponentially declining model.

4.2.1 Choosing the prior

One of the most relevant processes driving the evolution of galaxies is star formation. Besides other quantity, the first two physical parameters immediately coming in mind, because intimately related to star formation, are: stellar mass and star-formation rate. As largely reiterated in Chapter 3, measurements of $M_\star$ and $SFR[M_\star/yr]$ provide important information about the evolution of the galaxy.

To fit galaxy spectral energy distributions (SEDs), a model is generated and used. However, it is worth mentioning that the model includes a star formation history (SFH). Therefore, the fitted SFH is employed to derive physical parameters (Table 4.1).

This implies that the user cannot explicitly set the priors on these quantities because they are already implicitly set by the priors given for the SFH: SFH priors affect outcomes of the
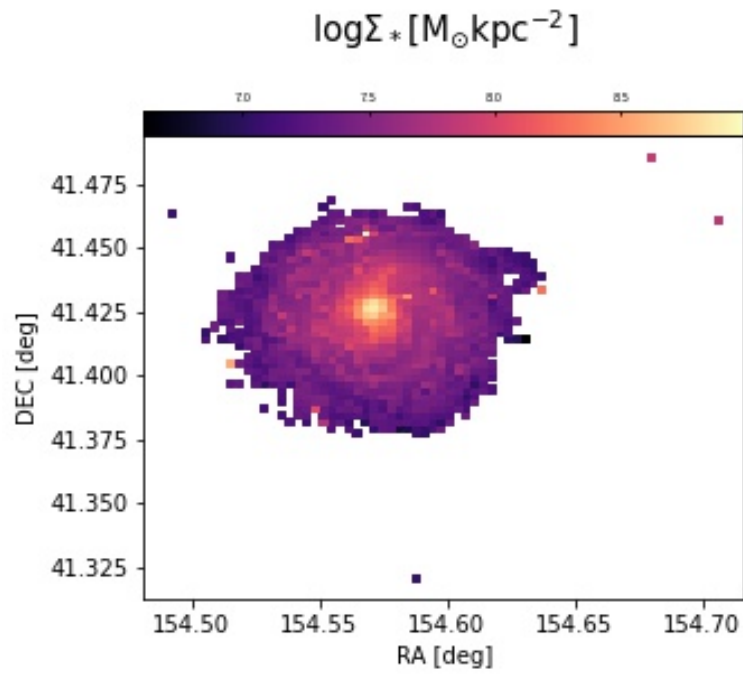
$$\log \Sigma_* [M_\odot \mathrm{kpc}^{-2}]$$

Figure 4.7: NGC3184: cells log stellar mass.

$$\log \Sigma_{\mathrm{SFR}} [M_\odot \mathrm{yr}^{-1} \mathrm{kpc}^{-2}]$$
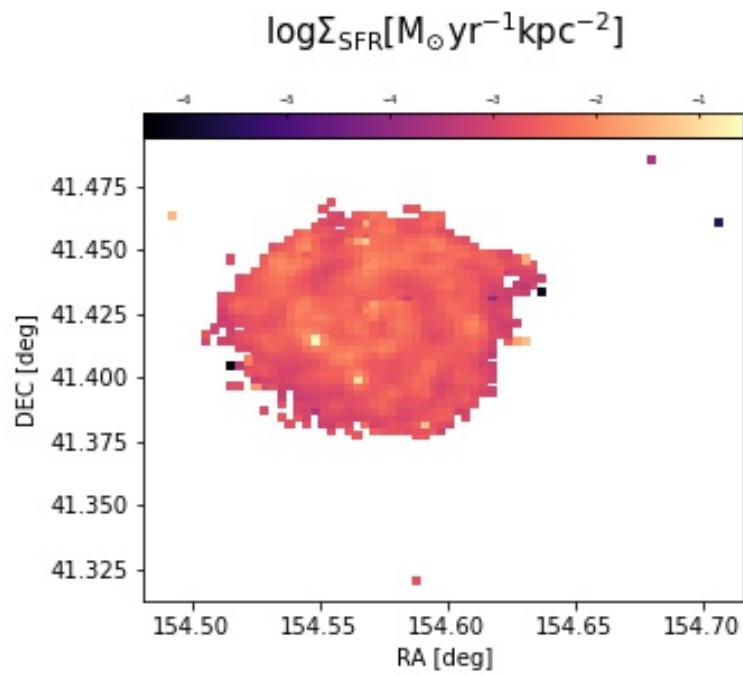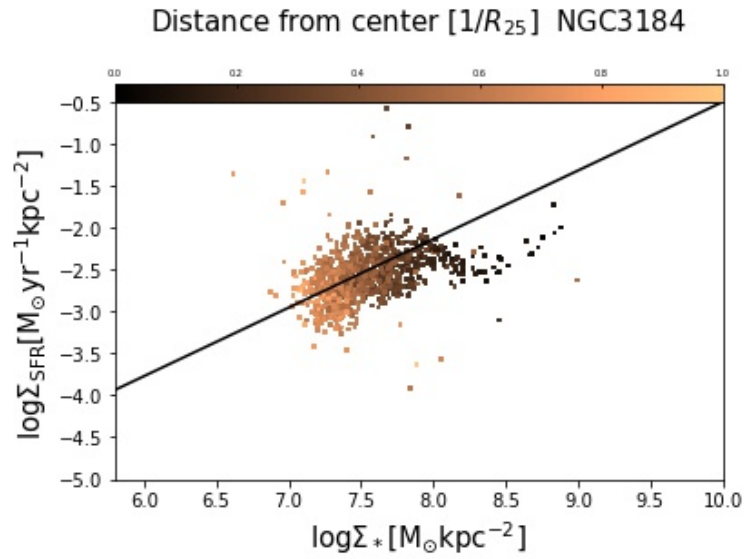

Figure 4.8: NGC3184: cells log star formation rate.

Figure 4.9: NGC3184: $\log \Sigma_\star$-$\log \Sigma_{\text{SFR}}$ plane. Cells are color-coded according to the distance from the galaxy center in units of r25. The black solid line is the MS (Eq 3.18).
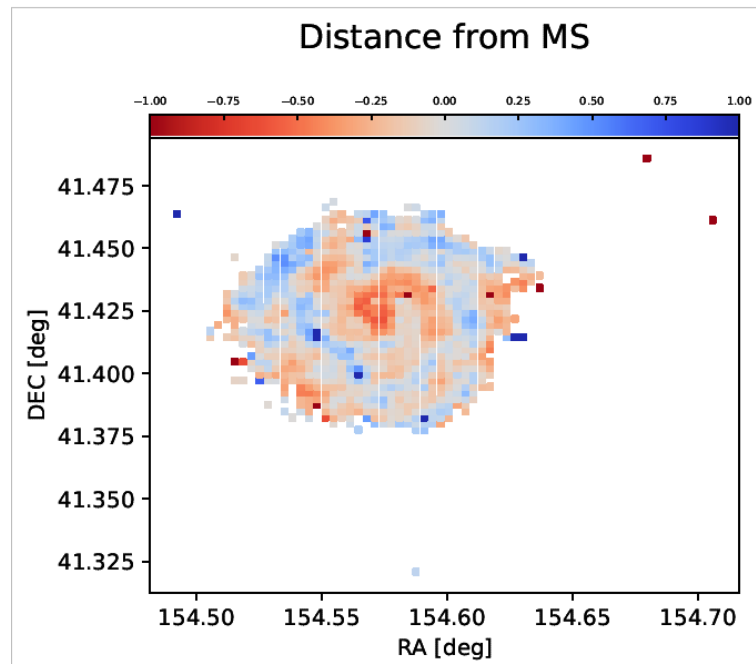

Figure 4.10: NGC3184: cell distance from the MS.

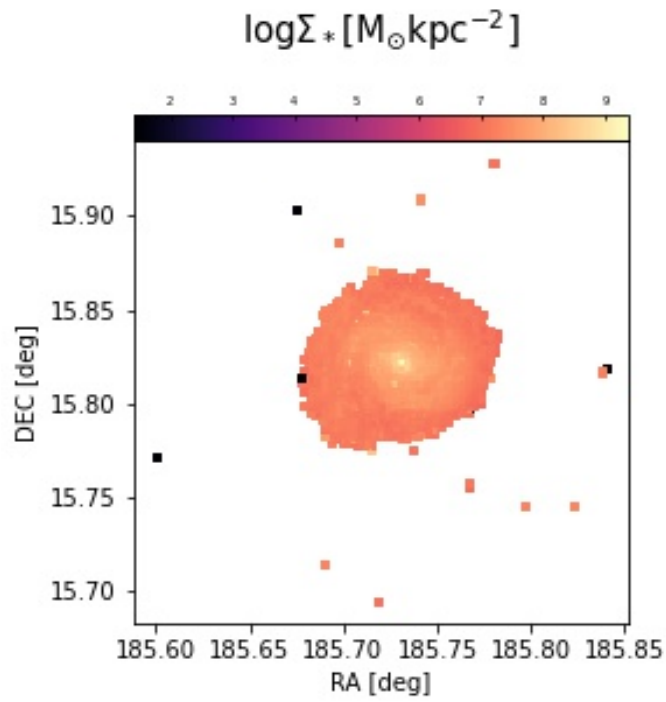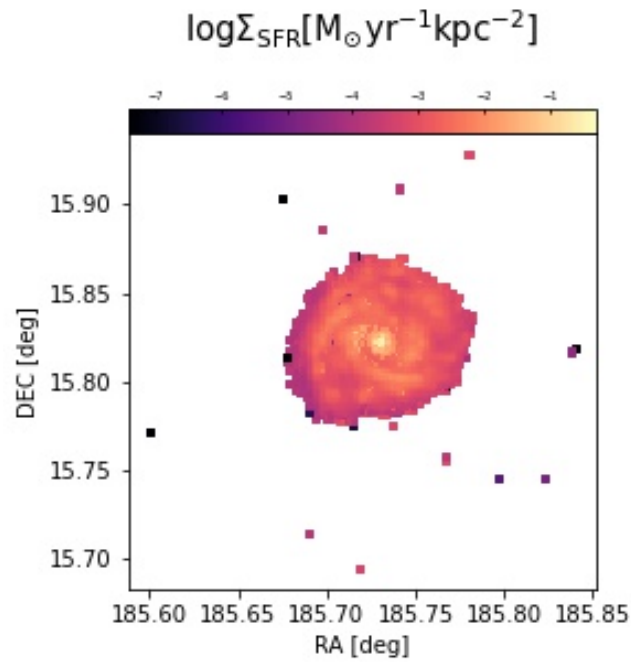Figure 4.11: NGC4321: cells log stellar mass.

Figure 4.12: NGC4321: cells log star formation rate.

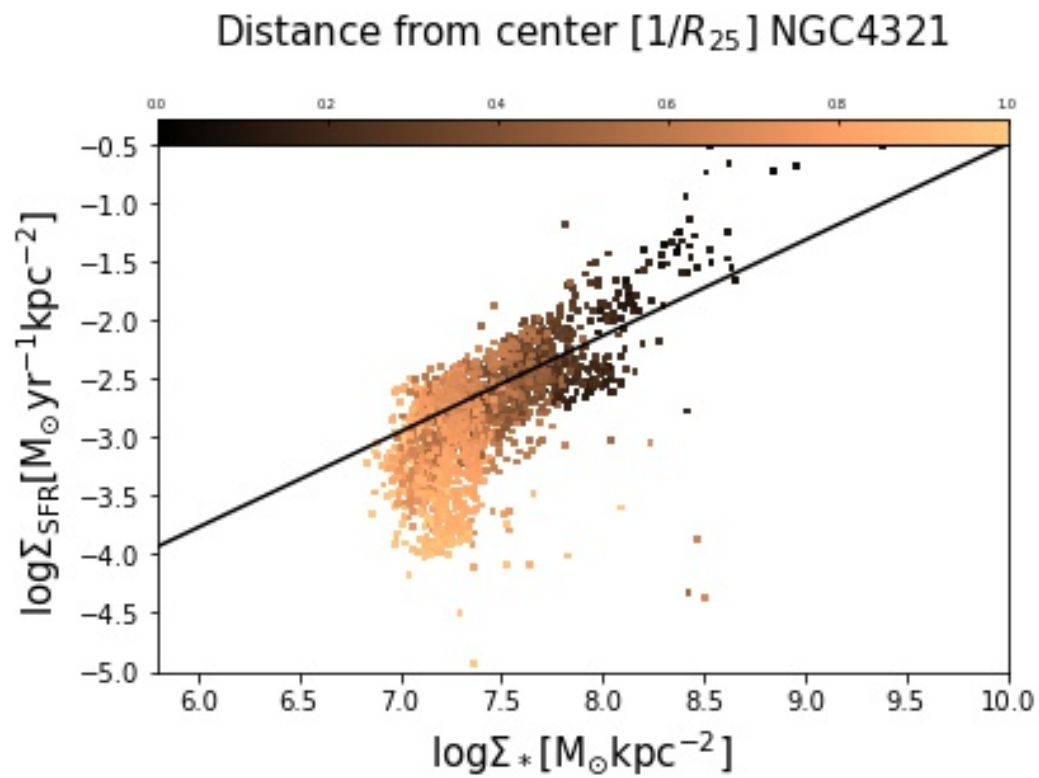Figure 4.13: NGC4321: $\log \Sigma_\star$-$\log \Sigma_{SFR}$ plane. Cells are color-coded according to the distance from the galaxy center in units of r25. The black solid line is the MS (Eq 2.18)
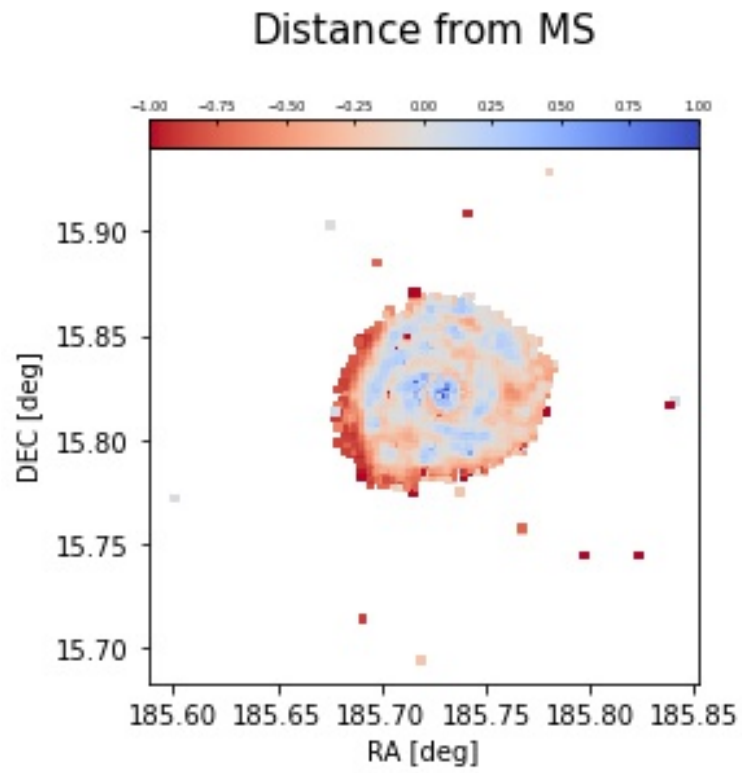
Figure 4.14: NGC4321: cell distance from the MS.

most crucial parameters holding information about the galaxy evolution.

The procedure is the following: choosing priors in a detached way so that they contain as less information as possible to obtain realistic and not external-affected outputs. The challenge is very hard to pursue because, in that case, the model should be capable of describing the data-generating processes and the data should constrain on the values of all model parameters and generally none of these two conditions are achievable.

Therefore, what remains to do, in this context, is to well examine the SFH priors in order to be as sensitive as possible and see if they are well justified. As will be shown in the following section, the parameter for the SFH model of this project, the Delayed exponentially declining model, is the timescale τ and the prior distribution chosen to be less informative as possible is the common uniform prior distribution:

$$P(\tau) \propto 1 \tag{4.13}$$

For each draw from the prior, by integrating the SFH multiplied by the mass-return function as a function of stellar age, the stellar mass $M_\star$ has been obtained. However, we recall that the stellar mass differs from the formed mass M_{formed}: the former is the current total mass in stars and remnants at time of observation, whilst the latter is total stellar mass formed during the galaxy lifetime. Actually, the dependence of $M_\star$ on the shape of SFH is weak, implying that the prior on $M_\star$ is independent of the parametric model used for SFH. If $M_\star$ is model-independent, the SFR relies on both the SFH model and the stellar mass. Yet, to remove the effect of the SFH model, the prior on sSFR will be considered, being equal to:

$$sSFR = \frac{SFR_{100}}{M_\star} \tag{4.14}$$

with SFR_{100} the last 100 Myr SFR, a "current SFH".

The second physical parameter is the mass-weighted formation time, t_{MW}, defined as the time (forwards measured) at which stellar masses of galaxies were assembled:

$$t_{\mathrm{MW}} = \frac{\int_0^{t_{\mathrm{obs}}} t SFR(t)\, dt}{\int_0^{t_{\mathrm{obs}}} SFR(t)\, dt} \tag{4.15}$$

It can be shown that changing the prior distribution significantly affects the two parameter above mentioned. Considering the parametric model chosen for this thesis, two different alternative prior probability densities can be discussed and compared to the uniform prior on τ.
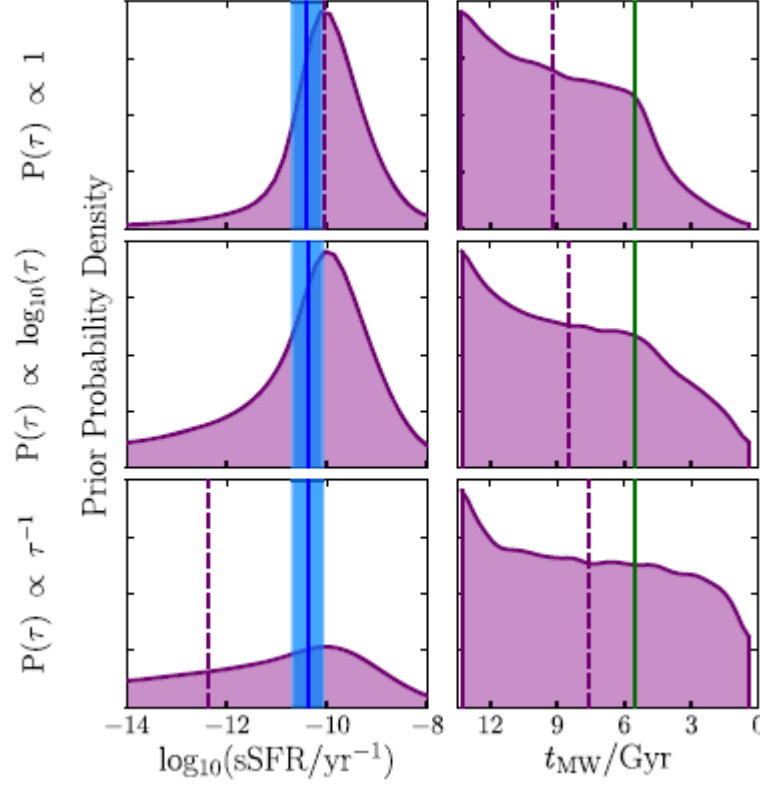
Figure 4.15: Priors imposed on sSFR and mass-weighted formation time by the exponentially declining SFH model under the assumption of different prior probability densities for the τ parameter. the prior medians are shown as dashed purple lines. The blue solid line is the z=0 SFMS of Speagle et al. (2014) for a stellar mass of $M\star= 10^{10.5} M_\odot$. The blue shaded region shows a scatter of 0.3 dex. The mass-weighted formation time for the stars in the universe, derived from the Madau & Dickinson (2014) SFRD curve, is shown as a solid green line

$$P(\tau) \propto \tau^{-1} \tag{4.16}$$

and

$$P(\tau) \propto \log_{10}(\tau) \tag{4.17}$$

By comparing priors imposed on sSFR and mass-weighted formation time, it is possible to conclude that, when using the exponentially declining SFH model, a prior probability density of $P(\tau) \propto 1$ produces a less informative prior on the parameters of interest than the more common uniform prior distribution $P(\tau) \propto 1$.

4.2.2 Parametric SFH models

In this section, two parametric models for star formation history will be discussed: exponentially declining model (Mortlock et al. 2017; McLure et al. 2018; Wu et al. 2018) and delayed exponentially declining model (Chevallard et al. 2019; Ciesla et al.2017). As reported many times, the second one is the model adopted for this project, still, since the two model show several analogies, the exponentially declining model will be analysed as well.

Exponentially declining model

The most applied for SFH model, it is also know as the "tau model": star-formation is assumed to jump from 0 to its maximum valeu at some time T_0 after which star formation declines exponentially with timescale τ

$$SFR(t) \propto \begin{cases} exp\left(-\frac{t-T_0)}{\tau}\right) & t > T_0 \\ 0 & t < T_0 \end{cases} \tag{4.18}$$

Though widely diffused, they have been shown to become less appropriate at higher redshifts (e.g., Reddy et al.2012), as they cannot reproduce rising SFHs and to produce biased estimates of stellar mass, SFR and mass-weighted age when used to fit observations of simulated galaxies (e.g., Simha et al. 2014; Pacifici et al. 2015; Carnall et al. 2018).

Delayed Exponentially declining model

Also known as the "delayed model", it is considered as an extension pf the previous model because the tau model SFR is multiplied by $(t - T_0)$ to remove both the discontinuity in SFR at $_{T0}$ in the tau model and the condition that star formation can only decline after that point. Furthermore, the more flexibility allows to reproduce rising SFHs if τ is large enough. This is the reason behind which the model has been chosen for the purpose of the thesis. The SFR can be written as:

$$SFR(t) \propto \begin{cases} (t - T_0)\, exp\left(-\frac{t-T_0)}{\tau}\right) & t > T_0 \\ 0 & t < T_0 \end{cases} \tag{4.19}$$

The prior probability densities for τ and $_{T0}$ is the same for both model and was described in the previous section.

Chapter 5

MAGPHYS vs BAGPIPES

In Chapter 2 and Chapter 3 we provided an overview of several plots with different physical parameters: stellar mass, $M_\star$, star-formation rate, SFR[$M_\star$/yr] and the derived Main Sequence (MS) relation (Eq. 3.18). Each of these parameters was obtained through the MAGPHYS and BAGPIPES code.

The aim of this chapter is to compare the $M_\star$ and SFR from the two independent codes, in order to show any potential discrepancy or correlation between them. We also briefly discuss potential offsets in terms of the Initial Mass Function (IMF) adopted in the codes, which may cause residual inconsistency in stellar mass and star-formation rate results.

5.1 Initial Mass Function

The initial mass function (IMF) is an empirical function which describes the initial distribution of masses for a population of stars. Since the IMF is an output of the process of star formation, it is strongly related to physical quantities such as stellar mass and star-formation rate. Let briefly sum up the definition of the IMF.

The mass function was originally defined by Salpeter (1955) as the number of stars N in a volume of space V observed at a time t per logarithmic mass interval $d\log m$:

$$\psi(\log m) = \frac{d(N/V)}{d\log m} = \frac{dn}{d\log m} \tag{5.1}$$

where $n = N/V$ is the stellar number density [pc $^{-3}$] From Eq. 5.1, Scalo (1986) defines the *mass spectrum* as the number density distribution per mass interval:

$$\psi(m) = \frac{dn}{dm} = \frac{1}{m(\ln 10)}\psi(\log m). \tag{5.2}$$

Then, if the mass function (Eq. 4.1) is approximated as a power law, the MF and the mass spectrum can be roughly written as:

$$\psi(\log m) \propto m^{-x} \tag{5.3}$$

and

$$\psi(m) \propto m^{-\alpha} \tag{5.4}$$

with α and $x = \alpha - 1$ as the two well-known exponents. Their original value given by Salpeter is $x = 1.35$ and $\alpha = 2.35$.

Generally, the IMF is described by a log-normal form for $m \leq 1M_\odot$ and power-law form for $m \geq 1M_\odot$ However, some observations suggest that the IMF is different in different environments. The most adopted IMF is the one by Chabrier, a log-normal form, (2003) and by Kroupa (2001), a broken power law. The two different expressions for the IMF are, also, the one used by, respectively, MAGPHYS and BAGPIPES and will be very shortly presented in the next section.

5.1.1 Chabrier and Kroupa IMF

As concerns the Chabrier IMF, for $m < 1M_\odot$, it is written as:

$$\psi(m) = 0.158(\frac{1}{\ln(10)m})\exp[-(\log(m) - \log(0.08))^2/(2x0.69^2)] \tag{5.5}$$

whilst, for $m > 1M_\odot$, it is written as:

$$\psi(m) = km^{-\alpha} \tag{5.6}$$

with $\alpha = 2.3 \pm 0.3$. Instead, the Kroupa IMF is a simple power law, wit the slope slightly changing at different mass intervals:

$$\psi(m) = m^{-\alpha}, \tag{5.7}$$

$$for\ m < 0.08M_\odot,\ \alpha = 0.3 \tag{5.8}$$

$$for\ 0.08 < m < 0.5M_\odot,\ \alpha = 1.3 \tag{5.9}$$

$$for\ m > 0.5M_\odot,\ \alpha = 2.3 \tag{5.10}$$

5.2   IMF comparison in MAGPHYS and BAGPIPES

Different assumptions of the initial mass function directly affect the stellar mass estimates, and the star-formation rate as well (SFR = $M_\odot$/yr). Usually this corresponds to a constant systematic offset between the physical paramaters computed in the different reference system. By integrating the Kroupa and Chabrier IMF, it can be shown that the calibration for the stellar masses is the following:

$$\log M_{\star,\,\text{Kroupa}} = \log M_{\star,\,\text{Chabrier}} + 0.04 \tag{5.11}$$

Thus, the difference in M_* computed with Kroupa and Chabrier (and so with BAGPIPES and MAPGPHYS) is very small, just 0.04dex, which is much smaller than the typical uncertainties in stellar masses due to the assumed models, stellar libraries and star formation histories ($\sim$0.2dex). For the direct comparison of the two codes, we then converted all outputs to the Chabrier IMF.

5.3   Stellar mass and SFR estimates: MAGPHYS and BAGPIPES

A comparison between stellar masses and SFRs obtained as MAGPHYS and BAGPIPES outputs are finally shown in Fig.5.1 and Fig.5.2. The stellar masses are almost consistent, with an average offset of ~ 0.005 dex and a scatter of 0.195 dex. For the SFR values, the discrepancy between the results from the two codes is only slightly larger: on average, the SFRs from MAGPHYS are $\sim$0.06 dex bigger than the ones from BAGPIPES with a scatter $\sim$0.28 dex.

We can then safely assume that the two codes provides consistent results for what concerns in particular the stellar mass. The agreement for the SFR from the two SED fitting procedures is also within the typical uncertainties from different SFR tracers. We note, however, that in this work for the SFR we rely on the observed UV+IR emissions, totally independent from the SED fitting analyses.
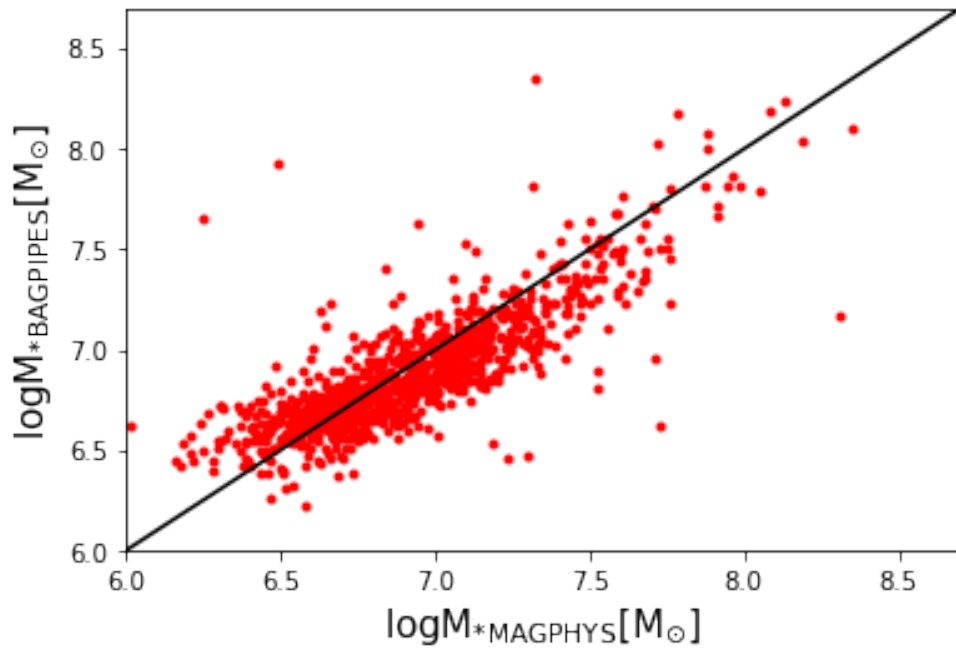
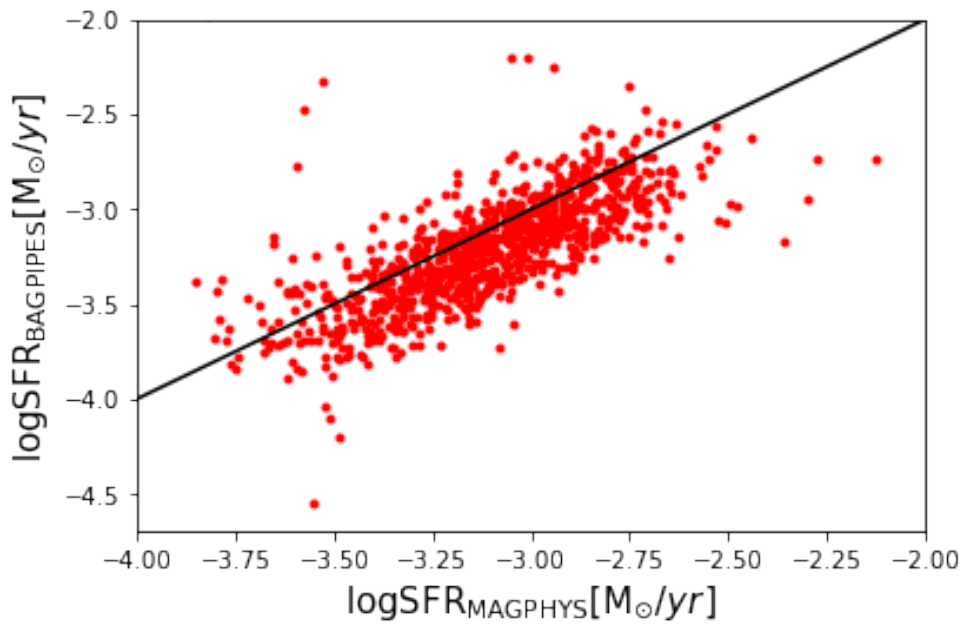Figure 5.1: Stellar mass, in log-log space, from MAGPHYS and BAGPIPES

Figure 5.2: Star-formation rate, in log-log space, from MAGPHYS and BAGPIPES

Chapter 6

Results and discussion: On the nature of stellar quenched rings in the outskirts of nearby grand design spirals

6.1   Summary

In this Thesis we have undertaken a comprehensive analysis of the spatially resolved Main Sequence of a couple of nearby grand design spiral galaxies. As mentioned in the Introduction, while on average a global scaling relation has been observed when combining a statistical sample of sources (e.g. Enia et al. 2020, Vulcani et al. 2020, Ellison et al. 2021), some objects can reveal peculiar features that are not observed in other sources. The motivation of my work is to understand the origin of significant deviations from the average MS observed in the sample of Enia et al. (2020). We have limited our analysis to two sources, as a pilot program to test the methodology that we plan to extend in the future to a much wider galaxy sample from the Dustpedia database.

6.2   A red and dead stellar ring surrounding NGC 4321

In this Section we discuss the implications of the SED fitting results from the BAGPIPES code. We have already shown how the assembled stellar mass and the ongoing SFR are spatially
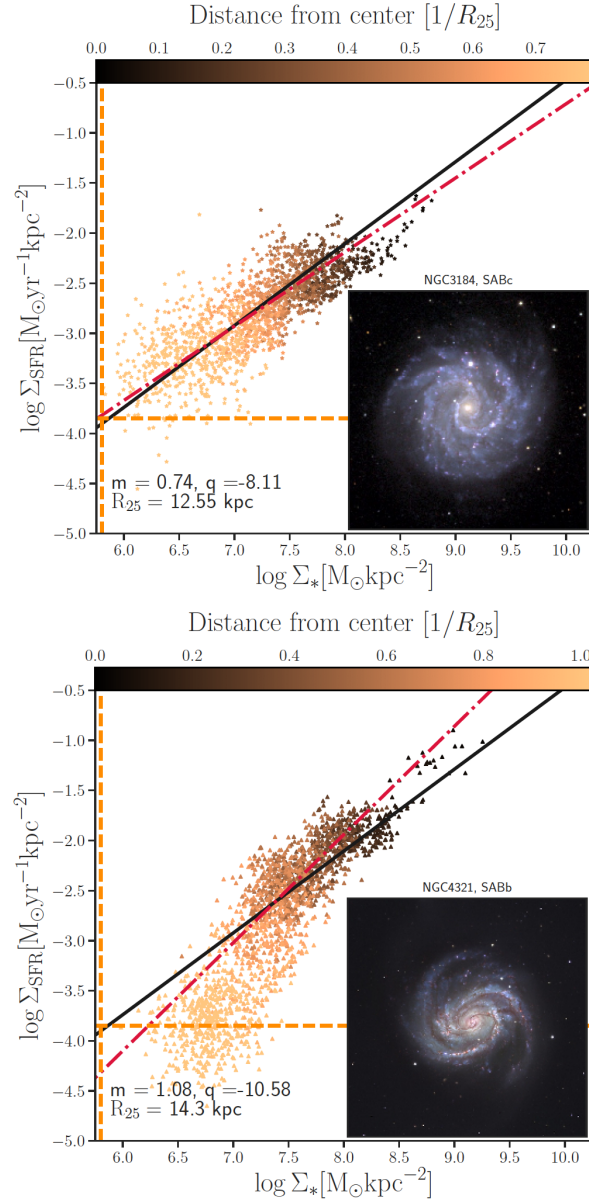
Figure 6.1: Summary of the spatially resolved MS for the two galaxies studied in this thesis. *Top panel:* the surface density of SFR is shown as a function of the stellar mass surface density for NGC 3184. The colors distribution encodes the distance from the center of the galaxy. The black line is the (total fitted) MS, the red dashed line the ODR fit for the single galaxy points, orange lines the sensitivity limits, the inset an RGB image of the galaxy as observed in optical bands. *Bottom panel:* same as the left panel but for NGC 4321. The figure is adapted from Enia et al. (2020).

distributed in the two spirals (see Fig. 4.8 - Fig. 4.12). By selection (Enia et al. 2020), the galaxies analyzed in this Thesis represent the final product of secular processes converting the gas into stars. Spiral galaxies are built across the Hubble time: they form stars at a pacific rate (excluding merger events), driven by the density waves turbulence crossing the Interstellar Medium within the gaseous disks. The regulation of this smooth star formation mode is at the origin of the observed Main Sequence of star forming galaxies, holding at different spatial scales (from $\sim$0.5Kpc up to the whole galaxy). To remind the specific behaviors of our sources, we compare in Figure 6.1 the spatially resolved MS of NGC3184 and NGC4321 (as originally reported by Enia et al. 2020).

As it can be seen in the bottom panel, NGC4321 presents a bimodal distribution in the stellar mass-SFR relation: indeed, at $\log(\Sigma_*) > 7.0\,\mathrm{M_\odot kpc^{-2}}$ the data follow the average MS scaling relation. At lower stellar mass densities, a cloud of data sits well below the expected values: at fixed stellar mass the observed SFR is suppressed, indicating the existence of quenched galactic regions.

When looking at the original sample of height face-on spirals, we can identify four galaxies showing a candidate quenched ring (including NGC4321, together with NGC4254, NGC4535 and NGC5194). This corresponds to 50% of the total. Even within the limited statistic available to us, it is clear that this peculiar feature is not so rare. It is thus crucial to characterize the physical properties of the stellar populations living in these under-dense and passive external regions of the galaxies.

We have then explored what information can be drawn from a systematic study of the star formation histories across NCG3184 and NGC4321, taking advantage of the performances of the BAGPIPES fitting procedure described in the previous chapters. For this Thesis, we restrict our analysis to a conservative case, adopting just one parametric description of the SF history: the delayed exponentially declining model (see Section 4.2.2) with additional random bursts, which provides an overall satisfactory consistence with the MAGPHYS code (as demonstrated in Chapter 5) . We demand to a future work the exploration of different parameterizations of the SF histories, including a non-parametric approach. Anyway, the main point here is to put ourselves into a common reference system, observing any systematic variations that could rise up in different environments of the galaxies. In this Section we report the results for the

two main parameters describing the shape of the delayed model: the formation time, t_{form}, and the timescale τ.

In Figure 6.2 we present, with the same format of the previous Chapters, the spatial distribution of t_{form} (counted as the time passed between the Big Bang and the epoch of birth of the galaxy) for NGC3184 (top panel) and NGC4321 (bottom panel). Similarly, in Figure 6.3 we report the distribution of τ.

Before attempting any interpretation, we have performed a careful visual investigation of the significance of the quenched ring in NGC4321, to avoid the possibility that it is related to a low Signal-to-Noise contamination in the optical/near-IR bands. However, we remind that only the pixels with a SNR>2 in at least 10 photometric bands have been considered for the SED fitting runs. Indeed, Figure 6.4 shows the near-infrared emission probed by the IRAC 3.6 μm *Spitzer* image, a direct tracer of the stellar mass. The two panels report the same map, but using different cut levels of the intensity contrast. Clearly, NGC4321 shows a faint and diffuse starlight emission toward the outskirts, highlighting the existence of old stars in these regions. In the right panel, where we can appreciate the extension of the spiral structure of this object, we overplot as small open white squares the positions of the cells that correspond to the passive cloud below the MS in Fig. 6.1 (bottom panel). Clearly, the round distribution of these points at large galactocentric distances correspond to the diffuse emission visible in the left panel, probing the existence of an extended population of old stars in the outer edges of the disk of NGC4321, with no evidence of ongoing SF processes. Interestingly, the red and dead zone begins almost exactly where the spiral arms end. We will go back to this observation in the final discussion.

6.3 Properties of the quenched ring

Figures 6.2 and 6.3 introduce the results of the variation of the key parameters of the SF histories derived from the SED fitting within the two sources: t_{form} and τ, respectively. For example, a visual inspection of these maps reveals an old stellar component at the center of NGC3184, corresponding to the stellar populations building the galactic bulge. NGC4321 has a less pronounced central region, while the most flashy feature that can be distinguished is a
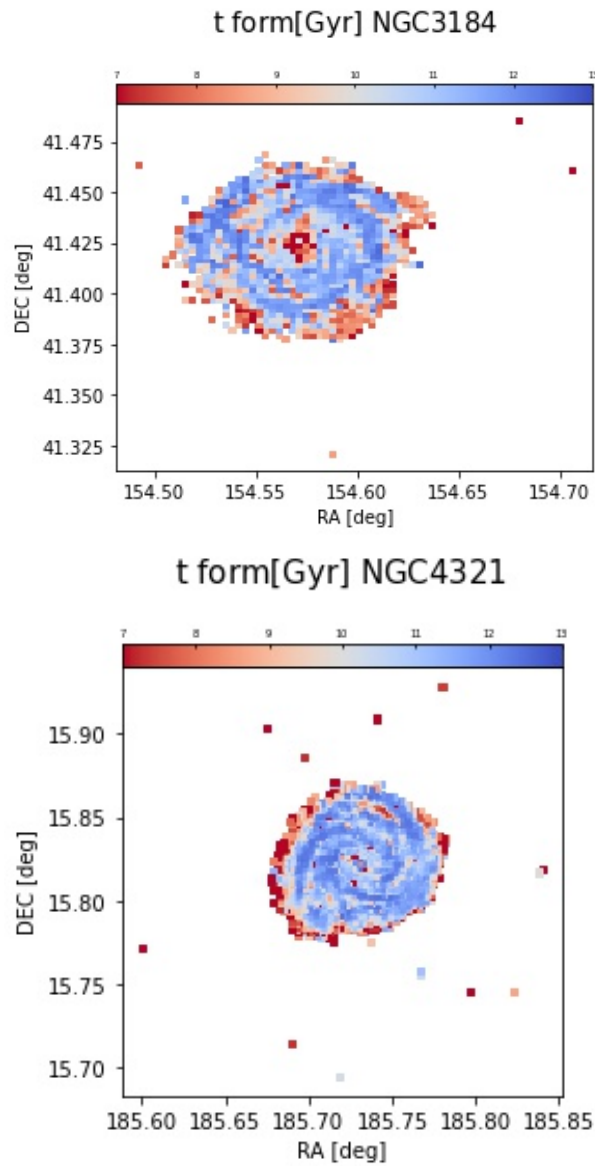
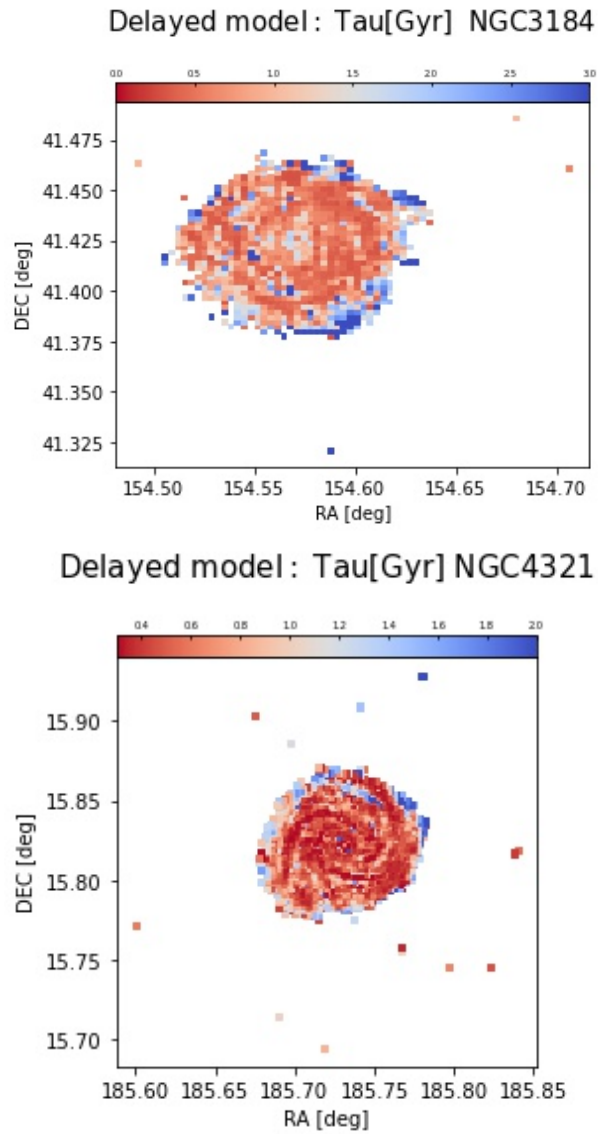Figure 6.2: Spatial distribution of t_{form} for NGC3184 and NGC4321, from the SED fitting of BAGPIPES.

Figure 6.3: Spatial distribution of τ for NGC3184 and NGC4321, from the SED fitting of BAG-PIPES.
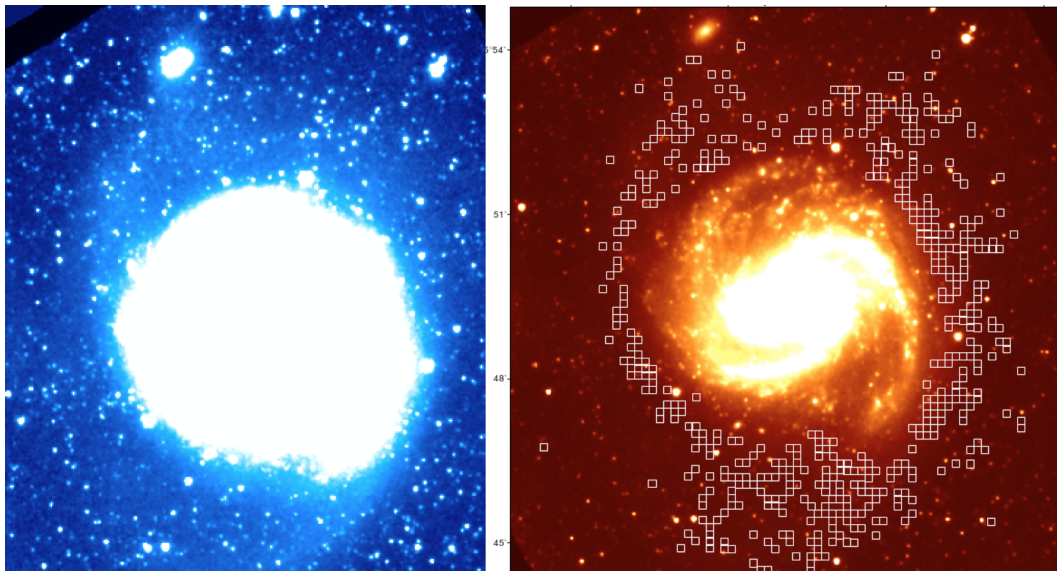
Figure 6.4: An IRAC/Spitzer view of the face-on galaxy NGC4321. The same map at 3.6μm is shown with different contrast parameters. *In the left panel* the image highlights the diffuse stellar emission around the disk. *On the right panel* we tune the image to show the structure of the spiral arms and the positions of the physical cells associated to the quenched ring (open white squares).

peripheral region surrounding the whole galaxy with formation times older then the rest of the object. This is the quenched ring already identified through its suppressed specific SFR. However, it is very difficult to draw any quantitative conclusion based on these maps. We have therefore tried to study the average radial profiles of t_{form} and τ. To do that, we have computed the distance of each physical cell from the center of the parent galaxy. By dividing the spatial extension of the disks in a grid of bins of distance (from the center up to the outskirts), we have averaged the values of t_{form} and τ for all the cells sitting in the different radial intervals. The results are reported in Figure 6.5 for t_{form} (top panel) and τ (bottom panel, see caption for a description of the symbols). The galactocentric distances are normalized to the R25 radius (i.e. the radius where the isophotal surface brightness in the B band reaches a value of 25.0 mag/arcsec^2, as reported in the Dustpedia public database) for a more meaningful comparison of sources with different physical sizes. Uncertainties are computed as the error on the mean value in each bin.

By looking at the average distribution of the formation times (computed again in units of time after the Big Bang) we observe an overall similar trend for the two spirals: excluding the very central bin, where NGC3184 shows an older t_{form} of ∼7 Gyrs, both galaxies present more recent stellar populations up to R=(0.5-0.8)R25, where the disk component dominates over the central bulge. In the outer regions t_{form} drops (more steeply for NGC3184), toward smaller values (i.e. older formation ages). Taking into account that at R>R25 even the statistics dramatically drops (changing from hundreds of cells to few units), we can derive a broad and general result: the stellar populations living in regions external to the optical radius are on average older then those of the disk component (at least for these sources). The most striking confirmation comes, however, from NGC4321, which shows a more extended and "dead" disk (up to R=2.5R25) than NGC3184.

We note that this scenario looks counterintuitive with respect to the predictions of the inside-out quenching mechanism, widely discussed in the literature to explain the formation of bulges in the local Universe (e.g. Morselli et al. 2019, among many others). Indeed, high-z observations find that, in the most massive galaxies, star formation is quenched from the inside out, on time scales less than 1 billion years in the inner regions, up to a few billion years in the outer disks. These galaxies sustain high star-formation activity at large radii, while
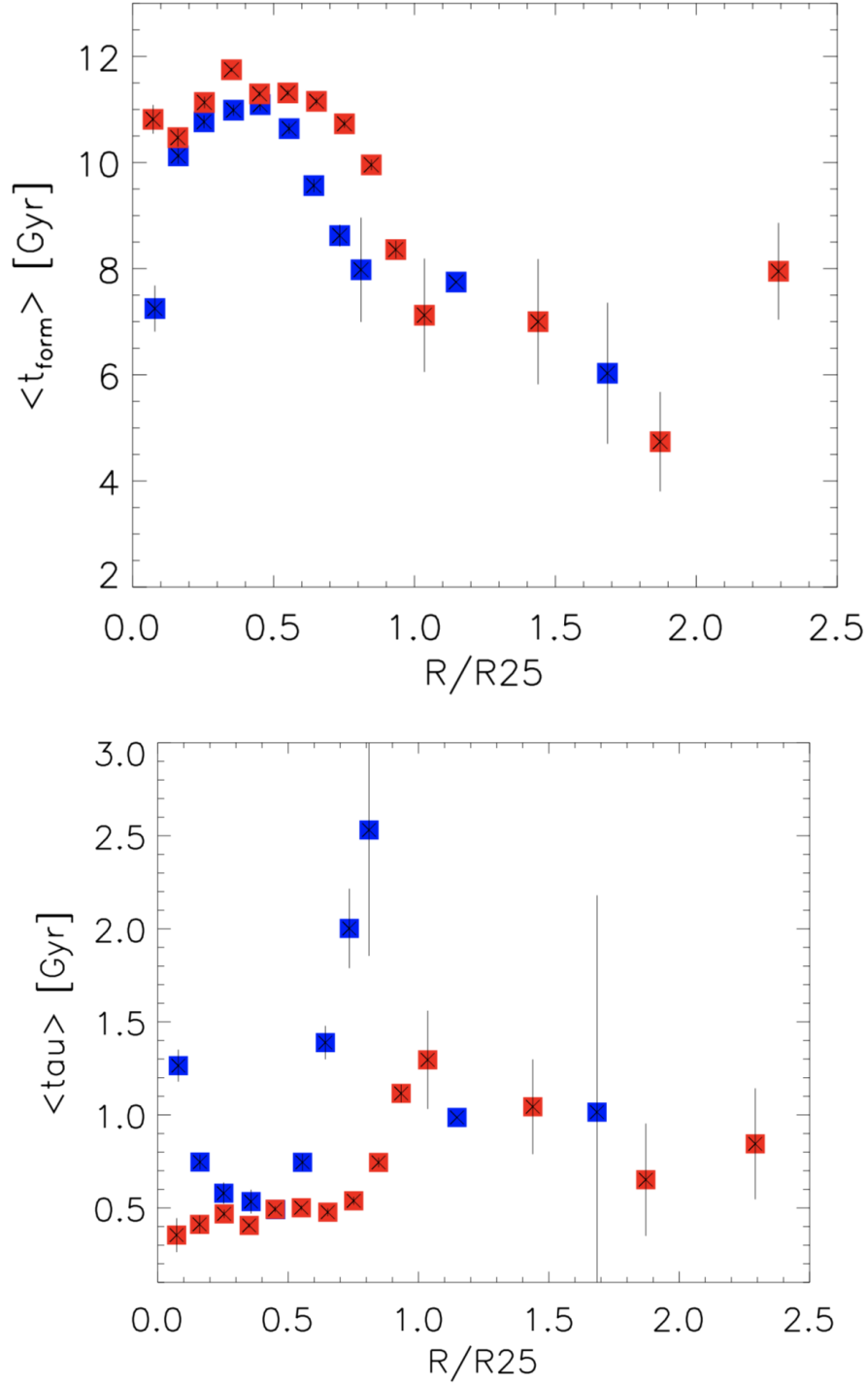
Figure 6.5: *Top panel:* Average radial distribution of t_{form}. Red squares refer to NGC4321, while blue squares indicate NCG3184. Uncertainties are computed as the error on the mean value in each bin. *Bottom panel:* Average radial distribution of τ. Symbols as in the top panel.
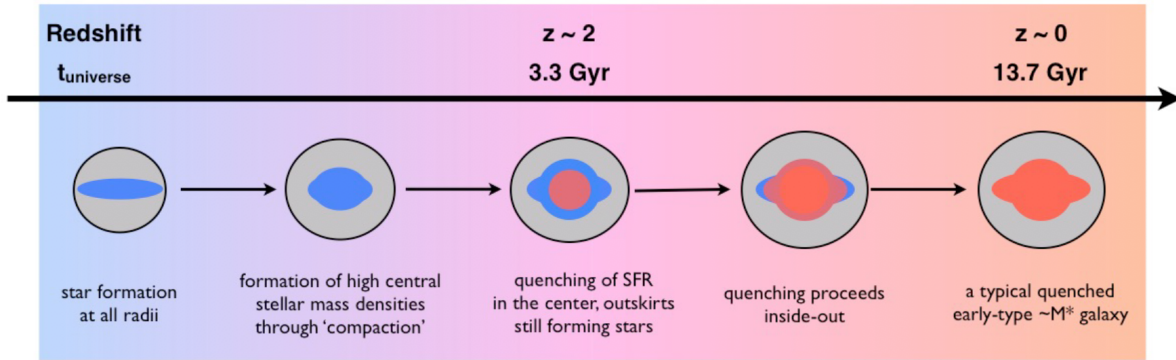
Figure 6.6: Inside-out quenching: proposed sketch of the evolution of massive galaxies. In this picture the total stellar mass and bulge mass grow synchronously in $z \sim 2$ main sequence galaxies, and quenching is concurrent with their total masses and central densities approaching the highest values observed in massive spheroids in today's universe. Model from Tacchella et al. (2015).

hosting fully grown and already quenched bulges in their cores (Tacchella et al. 2015). If this is observed at Cosmic Noon ($z \sim 2$), extrapolations at $z = 0$ could naively predict that the progressive quenching of SFR toward the edges of the disks will end up into an almost passive spheroid as of today (the toy model proposed by Tacchella et al. 2015 is shown in Fig. 6.6).

Within the optical radius, the inside-out scenario is reasonably consistent with our result, in particular if we observe the radial distribution of the timescale parameter τ (bottom panel of Fig. 6.5): τ is on average smaller at R<(0.5-0.8)R25 with typical values of $\sim$0.5Gyrs, while it increases up the R25 ($\tau \sim$1-3 Gyrs). Farther then the optical radius, the intringuing results from BAGPIPES found a new decrease of τ, again pointing to the existence of an extended distribution of old stars born through a short episode of SFR in the primordial Universe.

The origin of this external zone filled by old stars is still unconstrained.

6.4 Possible scenarios for the formation of the quenched rings

A thoughtful determination of the formation channels of these quenched rings would require more accurate follow-ups of the galaxy outskirts, to ideally constrain the properties of
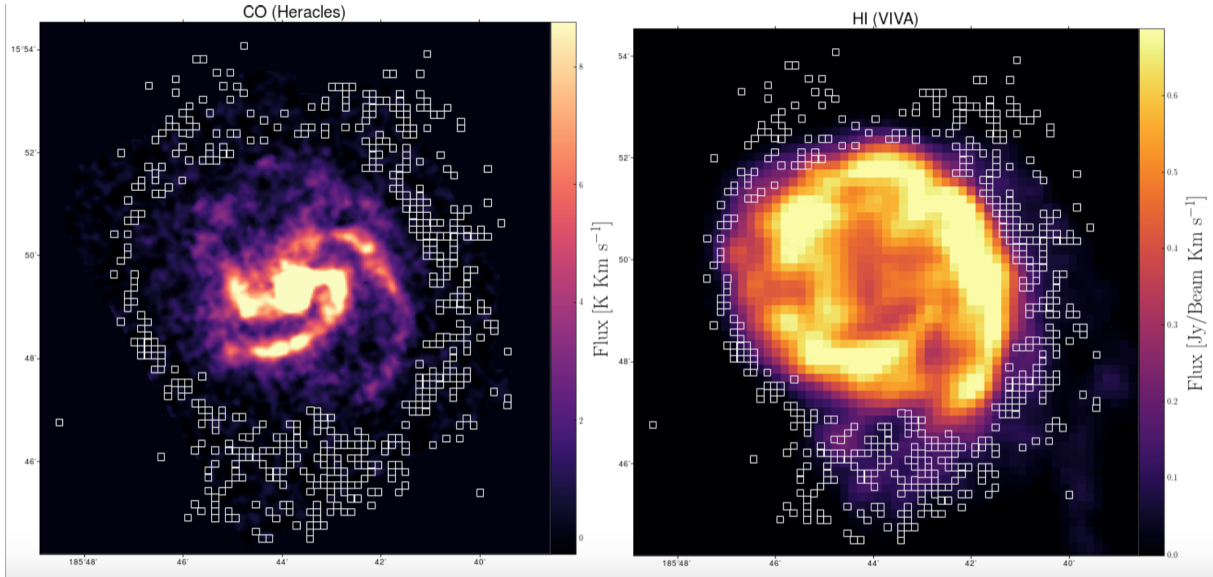
Figure 6.7: *Left panel:* The H2 gas phase for NGC4321 is traced by the CO emission from the Heracles survey. *Right panel:* HI emission from the public VIVA database. The maps are reported on the same astrometric system. The open squares mark the position of the galaxy cells building the quenched ring.

the stellar populations (ages, metallicitiy, extinction) from spectroscopic diagnostics in the UV, optical and near-IR.

However, here we briefly mention some possible interpretations based on the results reported in this Thesis. The main debate concerns if the formation process happened in-situ or ex-situ.

6.4.1   In-situ build-up:

- As mentioned in the previous Section, the existence of and old circumgalactic stellar population is not predicted by the classical inside-out quenching mechanism. However, given the symmetrical distribution of the quenched ring just outside of the optical radius, it is reasonable to consider that it could be associated to the primordial formation of the galaxy. This is supported by the observed distribution of other components of the Interstellar Medium, like the neutral (HI) and molecular (H2) hydrogen. These are presented in Figure 6.7. The H2 gas phase is here traced by the CO emission from the HERACLES

survey (The HERA CO-Line Extragalactic Survey, Leroy et al. 2009), while the HI comes from the public VIVA database. The maps are reported on the same astrometric system. The open squares mark the position of the galaxy cells building the quenched ring. Impressively, at this location the CO emission is completely lacking, while the atomic HI halo is still present. This could suggest that at early times an efficient burst triggered the birth of stars, with the consequent generation of intense stellar winds that were able to dissociate the H2 molecules (fuel for the SFR), leaving the primordial reservoir of HI. However, explaining the origin of such an external starburst is quite challenging.

- The bimodal distribution of the spatially resolved MS for NGC4321 can be interpreted as a bimodal SFR mode. The MS SFR mode is associated to the secular smooth processes in disks (both at low- and high-z). If the turbulence induced by the density waves triggers a constant SFR (at fixed cosmic time), we can think that at the formation epoch of the galaxy the spiral arms were more extended then we observe today. This could be induced by external tidal forces. A mismatch of the original disk area affected by the density waves with what we observe today, could have left a fossil record of the secular SFR processes at the edges of the galaxy.

- An unlikely possibility that we have considered is the migration of old stars born within the optical disk toward the outskirts.

6.4.2   Ex-situ formation:

- According to cosmological models, to sustain their SFR across the Hubble time, galaxies are fed by cold streams of primordial hydrogen. The way in which the gas is accreted (co-planar to the disk? perpendicular? e.g. Boucheé et al. 2017) affects the angular momentum of the whole source. The detection of the residual HI gas at the outer side of NGC4321, co-spatial to the quenched ring, puts a question mark about a possible correlation with the interaction of the pristine gas flowing within the galaxy.

- NGC4321 sits in the Virgo cluster, thus this galaxy is surrounded by the Intra Cluster Medium (ICM). Ram pressure stripping from the diffuse plasma is well know to deplete

the gas from galaxies flying within a cluster, quenching the ongoing SFR (e.g. Poggianti et al. 2017 and 2019). Therefore, it is natural to hypothesize a causal connection between the quenched ring and the environment quenching. However, other sources from the Enia et al. (2020) sample present a similar passive structure around the spiral galaxies (in particular M51), showing very similar trends as NGC4321 (in particular the coherent connection of the HI and the quenched stellar populations). These objects are not associated to any cluster, but dynamical interactions with a companion source in the past could have produced a similar perturbation.

- Major or minor merging with a spheroidal galaxy, redistributed around the spiral (to be tested against simulations, e.g, Bournaud et al. 2011).

6.5   Future perspectives

Given that in this Thesis I have studied only two sources, no definitive conclusions can be drawn, requiring a more statistical investigation on a larger sample of galaxies available from the Dustpedia database. We also plan to include different parameterization for the Star Formation histories, in particular the non-parametric models. We are also in the position of preparing future observational campaigns to add key data to unravel the tale of the external stellar populations that we have presented. Finally, it is mandatory to analyse large cosmological hydrodynamic simulations to identify if such red and dead stellar outskirts are produced in the models, in order to probe their dynamical origin.

References

Abdurro'uf & Akiyama M., 2017, MNRAS, 469, 2806

Abdurro'uf & Akiyama M., 2018, MNRAS, 479, 5083

Allamandola L. J., Hudgins D. M., Sandford S. A., 1999, ApJ, 511, L115

Allamandola L. J., Tielens A. G. G. M., Barker J. R., 1985, ApJ, 290, L25

Anders E., Grevesse N., 1989, Geochimica Cosmochimica Acta, 53, 197

Bouche' N. et al., 2017, arXiv:1612.00740

Bournaud et al. 2011, ApJ, 730, 4

Bradley L., et al., 2019, astropy/photutils: v0.6, doi:10.5281/zenodo.2533376, https://doi.org/10.5281/zenodo.2533376

Bruzual G., Charlot S., 2003, Monthly Notices of the Royal Astronomical Society, 344, 1000

Byler N., Dalcanton J. J., Conroy C., Johnson B. D., 2017, ApJ, 840, 44

Buchner J., et al., 2014, A&A, 564, A125

Calzetti D., Armus L., Bohlin R. C., Kinney A. L., Koornneef J., Storchi-Bergmann T., 2000, ApJ, 533, 682

Cano-Diaz+16, ApJL, 821, L26

Cano-Diaz+19, MNRAS, 488, 3

Carnall, A. C., McLure, R. J., Dunlop, J. S., & Davé, R. 2018, MNRAS, 480, 4379

Chabrier G., 2003, PASP, 115, 763

Charlot S., Fall S. M., 2000, ApJ, 539, 718

Chevallard, J., Curtis-Lake, E., Charlot, S., et al. 2019, MNRAS, 483, 2621

Ciesla, L., Elbaz, D., & Fensch, J. 2017, A&A, 608, A41

Clark+18, A&A, 609, A37

Daddi+07, ApJ, 670, 156

Davies+17, PASP, 129

da Cunha E., Charlot S., Elbaz D., 2008, MNRAS, 388, 1595

de Vaucouleurs G., de Vaucouleurs A., Corwin Herold G. J., Buta R. J., Paturel G., Fouque P., 1991, Third Reference Catalogue of Bright Galaxies

Dwek E. et al., 1997, ApJ, 475, 565

Ellison, S. et al., 2021, MNRAS.501.4777

Enia A. et al., 2020, MNRAS 000, 1–14

Feroz F., Hobson M. P., 2008, MNRAS, 384, 449

Feroz F., Hobson M. P., Bridges M., 2009, MNRAS, 398, 1601

Feroz F., Hobson M. P., Cameron E., Pettitt A. N., 2013, preprint, (arXiv:1306.2144)

Flagey N., Boulanger F., Verstraete L., Miville Desch^enes M. A., Noriega Crespo A., Reach W. T., 2006, A&A, 453, 969

Foreman-Mackey D., Hogg D. W., Lang D., Goodman J., 2013, PASP, 125, 306

Forster-Schreiber+09, ApJ, 706, 1364

Forster-Schreiber+18, ApJS, 238, 21

Glazebrook K., 2013, PASA, 30, e056

Goodman J.,Weare J., 2010, Communications in Applied Mathematics and Computational Science, Vol. 5, No. 1, p. 65-80, 2010, 5, 65

Gould & Salpeter, 1963, AJ, 138, 393

Hsieh+17, ApJ, 851, L24

Inoue A. K., Shimizu I., Iwata I., Tanaka M., 2014, MNRAS, 442, 1805

Kennicutt R. C., Jr, et al., 2003, PASP, 115, 928

Kroupa, P., & Boily, C. M. 2002, MNRAS, 336, 1188

Krumholz+11, ApJ, 731, 1, 25

Law+09, ApJ, 697, 2057

Leger A., Puget J. L., 1984, A&A, 137, L5

Leger A., D'Hendecourt L., Defourneau D., 1989, A&A, 216, 148

Leroy A. K., et al., 2009, AJ, 137, 4670

Madau, P., & Dickinson, M. 2014, ARA&A, 52, 415

Medling+18, MNRAS, 475, 5194

Morrissey P., et al., 2007, ApJS, 173, 682

Noeske+07, ApJ, 660, L47

Peng+15, Nature, 521, 192

Pilbratt G. L., et al., 2010, A&A, 518, L1

Planck Collaboration et al., 2016, A&A, 594, A13

Poggianti et al. 2017, ApJ, 844, 48

Poggianti et al. 2019, MNRAS, 482, 4466

Popesso+19, MNRAS, 483, 3213

Reddy, N. A., Pettini, M., Steidel, C. C., et al. 2012, ApJ, 754, 25

Renzini+15, ApJL, 801, L29

Rodighiero+11, ApJL, 739, L40

Rodighiero+14, MNRAS, 443, 1

Rosales-Ortega+12, ApJ, 756, L31

Saintonge+16, MNRAS, 462, 2

Sanchez+13, A&A, 554, A58

Schreiber+15, A&A, 575, A74

Sellgren K., 1984, ApJ, 277, 623

Simha, V., Weinberg, D. H., Conroy, C., et al. 2014, arXiv:1404.0402

Simons+17, ApJ, 843, 46

Skilling J., 2006, Bayesian Anal., 1, 833

Skrutskie M. F., et al., 2006, AJ, 131, 1163

Speagle, J. S., Steinhardt, C. L., Capak, P. L., & Silverman, J. D. 2014, ApJS, 214, 15

Tacchella+15, Science, 348, 6232

Übler+19, ApJ, 880, 48

Veilleux+05, ARA&A, 43, 1

Vulcani et al. 2020, ApJ, 899, 98

Werner M. W., et al., 2004, ApJS, 154, 1

Whitaker+14, ApJ, 795, 104

Wisnioski+15, ApJ, 799, 209

Wright E. L., et al., 2010, AJ, 140, 1868

York D. G., et al., 2000, AJ, 120, 1579